Open access • Journal Article • DOI:10.1088/0741-3335/54/7/074009

Minority and mode conversion heating in (3He)–H JET plasmas — Source link

D. Van Eester, E. Lerche, Thomas Johnson, Torbjörn Hellsten ...+41 more authors

Institutions: European Atomic Energy Community, Royal Institute of Technology, Uppsala University, Ghent University ...+4 more institutions

Published on: 20 Jun 2012 - Plasma Physics and Controlled Fusion (IOP Publishing)

Topics: Dielectric heating and Ion cyclotron resonance

Minority and mode conversion heating in (^{3}He)–H JET plasmas

2012 Plasma Phys. Control. Fusion 54 074009

(http://iopscience.iop.org/0741-3335/54/7/074009)

Plasma Phys. Control. Fusion **54** (2012) 074009 (19pp) doi:10.1088/0741-3335/54/7/074009

Minority and mode conversion heating in (^{3}He)–H JET plasmas

D Van Eester[1], E Lerche[1], T J Johnson[2], T Hellsten[2], J Ongena[1], M-L Mayoral[3], D Frigione[4], C Sozzi[5], G Calabro[4], M Lennholm[6], P Beaumont[3], T Blackman[3], D Brennan[3], A Brett[3], M Cecconello[7], I Coffey[3], A Coyne[3], K Crombe[8], A Czarnecka[9], R Felton[3], M Gatu Johnson[7], C Giroud[3], G Gorini[5], C Hellesen[7], P Jacquet[3], Ye Kazakov[10], V Kiptily[3], S Knipe[3], A Krasilnikov[11], Y Lin[12], M Maslov[13], I Monakhov[3], C Noble[3], M Nocente[5], L Pangioni[3], I Proverbio[5], M Stamp[3], W Studholme[3], M Tardocchi[5], T W Versloot[14], V Vdovin[15], A Whitehurst[3], E Wooldridge[3], V Zoita[16] and JET EFDA Contributors[17]

JET-EFDA Culham Science Centre, Abingdon, OX14 3DB, UK
[1] LPP-ERM/KMS, Association Euratom-'Belgian State', TEC Partner, Brussels, Belgium
[2] Fusion Plasma Physics, Association Euratom-VR, KTH, Stockholm, Sweden
[3] Euratom-CCFE Fusion Association, Culham Science Centre, UK
[4] Euratom-ENEA sulla Fusione, C. R. Frascati, Frascati, Italy
[5] Instituto di Fisica del Plasma, EURATOM-ENEA-CNR Association, Milan, Italy
[6] EFDA Close Support Unit, Culham Science Centre, Abingdon OX14 3DB, UK & European Commission, B-1049 Brussels, Belgium
[7] Uppsala University, Association EURATOM-VR
[8] Department of Applied Physics, Ghent University, B-9000 Ghent, Belgium
[9] Institute of Plasma Physics and Laser Microfusion, Warsaw, Poland, Uppsala, Sweden
[10] Chalmers University of Technology, Euratom-VR Association, Göteborg, Sweden
[11] SRC RF Troitsk Institute for Innovating and Fusion Research, Troitsk, Russia
[12] MIT Plasma Science and Fusion Center, Cambridge, MA 02139, USA
[13] CRPP-EPFL, Association Euratom-Confédération Suisse, CH-1015 Lausanne, Switzerland
[14] FOM Institute Rijnhuizen, Association EURATOM-FOM, Nieuwegein, the Netherlands
[15] RNC Kurchatov Institute, Nuclear Fusion Institute, Moscow, Russia
[16] Association EURATOM-MEdC, National Institute for Plasma Physics, Bucharest, Romania

Received 20 May 2011, in final form 12 August 2011
Published 20 June 2012
Online at stacks.iop.org/PPCF/54/074009

Abstract
Radio frequency (RF) heating experiments have recently been conducted in JET (^{3}He)–H plasmas. This type of plasmas will be used in ITER's non-activated operation phase. Whereas a companion paper in this same PPCF issue will discuss the RF heating scenario's at *half* the nominal magnetic field, this paper documents the heating performance in (^{3}He)–H plasmas at *full* field, with fundamental cyclotron heating of ^{3}He as the only possible ion heating scheme in view of the foreseen ITER antenna frequency bandwidth. Dominant electron heating with global heating efficiencies between 30% and 70% depending on the ^{3}He concentration were observed and mode conversion (MC) heating proved to be as efficient as ^{3}He minority heating. The unwanted presence of both ^{4}He and D in the discharges gave rise to 2 MC layers rather than a single one. This together with the fact that the location of the high-field side fast wave (FW) cutoff is a sensitive function of the parallel wave number and that one of the locations of the wave confluences critically depends on the ^{3}He concentration made the interpretation of the results, although more complex, very interesting: three regimes could be distinguished as a function of $X[^3\mathrm{He}]$: (i) a regime at low concentration ($X[^3\mathrm{He}] < 1.8\%$) at which ion cyclotron resonance frequency (ICRF) heating is efficient, (ii) a regime at intermediate concentrations

[17] See the appendix of Romanelli F *et al* 2010 *Proc. 23rd IAEA Fusion Energy Conference 2010 (Daejon, Korea).*

($1.8 < X[^3\mathrm{He}] < 5\%$) in which the RF performance is degrading and ultimately becoming very poor, and finally (iii) a good heating regime at ^{3}He concentrations beyond 6%. In this latter regime, the heating efficiency did not critically depend on the actual concentration while at lower concentrations ($X[^3\mathrm{He}] < 4\%$) a bigger excursion in heating efficiency is observed and the estimates differ somewhat from shot to shot, also depending on whether local or global signals are chosen for the analysis. The different dynamics at the various concentrations can be traced back to the presence of 2 MC layers and their associated FW cutoffs residing inside the plasma at low ^{3}He concentration. One of these layers is approaching and crossing the low-field side plasma edge when $1.8 < X[^3\mathrm{He}] < 5\%$. Adopting a minimization procedure to correlate the MC positions with the plasma composition reveals that the different behaviors observed are due to contamination of the plasma. Wave modeling not only supports this interpretation but also shows that moderate concentrations of D-like species significantly alter the overall wave behavior in ^{3}He-H plasmas. Whereas numerical modeling yields quantitative information on the heating efficiency, analytical work gives a good description of the dominant underlying wave interaction physics.

(Some figures may appear in colour only in the online journal)

1. Introduction

Before going to its activated phase, ITER will be operated using H or ^{4}He as majority species at 2.65 T (half field) and 5.3 T (full field). While the former rely on heating H ions at their fundamental ion cyclotron resonance or ^{3}He ions at their 2nd harmonic resonance, the latter is based on fundamental ICRF heating of a ^{3}He minority. From the ion cyclotron resonance frequency (ICRF) heating point of view, H–^{3}He plasmas at 2.65 T are an exact mock-up of D–T plasmas: The Z/A values of H and ^{3}He ions (Z: charge number, A: mass number) differ by a factor of 2 with those of D and T and hence the relative positions of the cyclotron layers of the main ion species in ITER's D–T phase are identical when running at half the field in H–^{3}He.

Recent JET experiments examined the various radio frequency (RF) heating schemes (^{3}He)–H plasmas that can be used in ITER. The potential of the fundamental ($N = 1$, where N is the cyclotron harmonic number) H majority heating and the second harmonic ($N = 2$) ^{3}He heating at ITER's half field was examined [1, 2]. ^{3}He will also play an important role in the activated phase of the next step machine, where it will be a small minority heated at its fundamental cyclotron frequency, its main role being to contribute—via Coulomb collisional slowing down of the moderately fast ion tail—to the bulk ion heating, and thus to significantly enhance the fusion reactivity for a given amount of wave injected ICRF power [3]. To get a feeling of the behavior of this minority, (^{3}He)–H mixtures will also be studied at the *nominal* magnetic field in ITER prior to the activated phase. In view of the limited bandwidth foreseen for the ITER antennas fundamental ^{3}He minority heating is the only RF ion heating scheme available for this ITER operation phase. By merely changing the magnetic field to the more standard 3.4 T in the recent JET experiments, minority and mode conversion (MC) wave heating in (^{3}He)–H plasmas could directly be studied, properly placing the ^{3}He minority cyclotron layer centrally in the plasma as it will be in ITER. In 'inverted' heating scenarios, e.g. in (^{3}He)–H, the ion–ion hybrid (IIH) layer is positioned between the antenna on the low-field side (LFS) and the ion cyclotron layer of the minority ions while in standard—e.g. (^{3}He)–D—heating scenarios the ion cyclotron layer is in between the IIH layer and the LFS. Mayoral *et al* examined the ICRF heating of (^{3}He)–H plasmas at very low ^{3}He concentrations (∼1%) [4] and found that the MC regime was already reached at $X[^3\mathrm{He}]$∼2–3%, in contrast to the ∼10–15% needed to make the MC efficient in non-inverted scenarios; the performance at somewhat higher ^{3}He concentrations was so far not yet explored although the wave dynamics in plasmas consisting of at least three ion species and giving rise to multiple MC layers—as will be the case in ITER—deserves attention. Mayoral's experiments also brought to light the sensitivity of inverted scenarios to the plasmas composition: The presence of small amounts of carbon in the plasma (up to 2010 unavoidable in JET plasmas as the machine's inner vessel was covered with C tiles) shifted the location of the MC layer over a distance of ∼0.2 m away from where it was expected for a (^{3}He)–H plasma without C. Work on Phaedrus-T revealed a similar sensitivity of the (Alfvén) heating performance on minute amounts of impurities, the electrons of which represent a non-negligible fraction of the total electron density thus indirectly influencing the wave propagation and damping characteristics [5]. From midyear 2011 onwards the JET first wall will be ITER-like and will predominantly consist of beryllium. Assessing the impact on the heating performance of modest amounts of first wall material impurities entering the plasma, and finding ways to control or mitigate adverse effects is also crucial when preparing for ITER.

MC rather than minority heating is taking place when injecting more than just a few per cent of ^{3}He in H plasmas. MC physics has been explored experimentally in many machines, including e.g. TFTR [6], ASDEX-U [7, 8] and Alcator C-mod [9, 10]. MC heating and MC-based wave-to-particle momentum transfer relies on the conversion, at the IIH resonance, of the FW launched by standard RF antennas, to shorter wavelength waves that are efficiently damped on electrons. Bounded plasma effects allow us to significantly enhance the MC and thereby the overall RF heating efficiency

when the machine and plasma parameters are chosen such that an integer number of FW wavelengths can be folded in between the high-field side (HFS) FW cutoff and the IIH layer. This effect was already experimentally identified in JET (^{3}He)–D plasmas [11] and was recently tested in JET (^{3}He)–H plasmas. The Tore Supra team demonstrated that MC heating can be as efficient as minority heating and pointed out the fact that the idea of constructive/destructive interference can be generalized to a global bounded plasma effect of an antenna in a metallic shell [12] (see also [13] for 1D modeling). Similar conclusions were drawn in the Alfvén frequency domain when studying wave propagation in the Phaedrus-T machine [14]. The recent JET experiments allowed getting a better insight in the MC dynamics of a multiple ion-species plasma.

MC heating has become one of the standard tools for transport analysis and is often used in rotation experiments (see e.g. [15, 16]). Although no consistent theoretical framework yet exists that solidly links the experimental evidence of flow driven on the one hand and the fate of the energy carried by the up–down asymmetric mode converted waves on the other hand, many believe that one of the main roles externally launched ICRF waves may play in future machines is to ensure flow drive which impacts on plasma confinement and stability. Although the present paper's main focus is on MC physics, a section is devoted to presenting experimental results of plasma rotation analysis in (^{3}He)–H plasmas.

The more recent (^{3}He)–H experiments studied both the low and high $X[^3\mathrm{He}]$ range and in particular addressed the question how the heating efficiency can be maximized by exploiting bounded plasma constructive interference effects. Since scanning the minority concentration moves the confluence layer positions significantly, the 'resonator' effect and its potential to enhance the MC heating efficiency could be examined.

This paper focuses on describing the recent (^{3}He)–H experiments and on explaining the observed heating efficiency. It is structured as follows: first, general information is given. Then the importance of the ^{3}He concentration, $X[^3\mathrm{He}]$, on the performance of the heating scenario is highlighted showing the dependence of some key experimental quantities on $X[^3\mathrm{He}]$. The response of the plasma to RF power modulation is the subject of the next section. Subsequently the sensitivity of the MC locations on the plasma composition is studied, and a section is devoted to wave-induced fast particle populations. A short section on the obtained rotation data is included. That section is intentionally purely descriptive; *no* effort being made to explain the observed effects from first principles. After that, a section is devoted to the wave modeling, explaining qualitatively how the MC physics impacts on the heating efficiency. Finally, conclusions are drawn.

2. Recent JET (^{3}He)–H experiments

2.1. General remarks

During the recent MC studies in JET in (^{3}He)–H plasmas two types of discharges were used alternatingly. One type of discharge was intended to assess the minority and MC heating performance while the focus in the others was the analysis of RF induced plasma rotation. In the former, the ICRF power was modulated throughout the flat top of the discharge and a modulation frequency of 4 Hz was used. In the latter, neutral beam injection (NBI) beam blips with a duration of 100 ms were used to assess the toroidal and poloidal bulk plasma rotation. For the first and last blip the injected D particles have an energy of 130 keV, while for the other blips the particles have an energy of 88 keV. As fast particles speed up the plasma by transferring their momentum through Coulomb collisions, the time intervals during which the diagnostic beam is fired are short compared with the flat top time. In between beam blips RF power modulation at 25 Hz was applied. No H beam was available and thus a D beam had to be used. Hence it is also necessary to assess how the ICRF power affects this D population and to have an idea of which fraction of the launched RF power is parasitically lost to particles that are only injected in the machine for diagnostic purposes.

The applied RF power level was typically ∼4 MW, reduced to half that value during slow modulation and to 15% of the maximal value during fast modulation. The 4 Hz slow modulation allows the study of the response of both the ion and of the electron temperature to the RF power level change. The electron temperature is obtained from electron cyclotron emission (ECE), while the ion temperature is obtained from charge-exchange measurements. Also global signals (such as the diamagnetic energy or the plasma energy) can be studied. The charge-exchange diagnostic beam is left on during the whole discharge during the first type of shots, while it is only operating for very limited periods of time during the second type of shots. The 25 Hz modulation is too fast to capture the ion dynamics and only allows studying the electron response. In spite of this drawback, the fast modulation is extremely useful as it is not suffering from the effects of heat wave diffusion away from the heat source and thus allows a better understanding of how the actual (be it only electron) power deposition profile looks like.

The applied frequency is ∼32 MHz and the toroidal magnetic field at the geometric axis ($R_\mathrm{o} = 2.97$ m) is $B_\mathrm{o} = 3.41$ T. Dipole $(0\,\pi\,0\,\pi)$ phasing is used for the four straps of the A2 antennas and a low triangularity plasma shape is chosen such that the last closed flux surface is as parallel as possible to the antenna straps to optimize coupling. With the modest auxiliary power input the plasma remains in L-mode. For the chosen parameters the $N = 1$ ^{3}He cyclotron layer is located ∼0.24 m to the LFS of the plasma core while the $N = 1$ H cyclotron layer is outside the machine on the LFS. The $N = 1$ D layer lies on the HFS but ICRF heated D beam particles will absorb wave power at their Doppler-shifted resonance layer, which is closer to the plasma core.

Figure 1 shows the time evolution of several key quantities of two discharges at different ^{3}He concentrations. The ^{3}He concentration (see figure 1(*d*)) is scanned from 1% to 4% in discharge #79343 and from 3% to 12% in shot #79352. In both discharges the response of the radiated power (figure 1(*b*)), the electron temperature (figure 1(*g*)) and the MHD energy (figure 1(*f*)) to the modulation of the ICRF power (figure 1(*a*)) is clearly visible while the response of the ion temperature

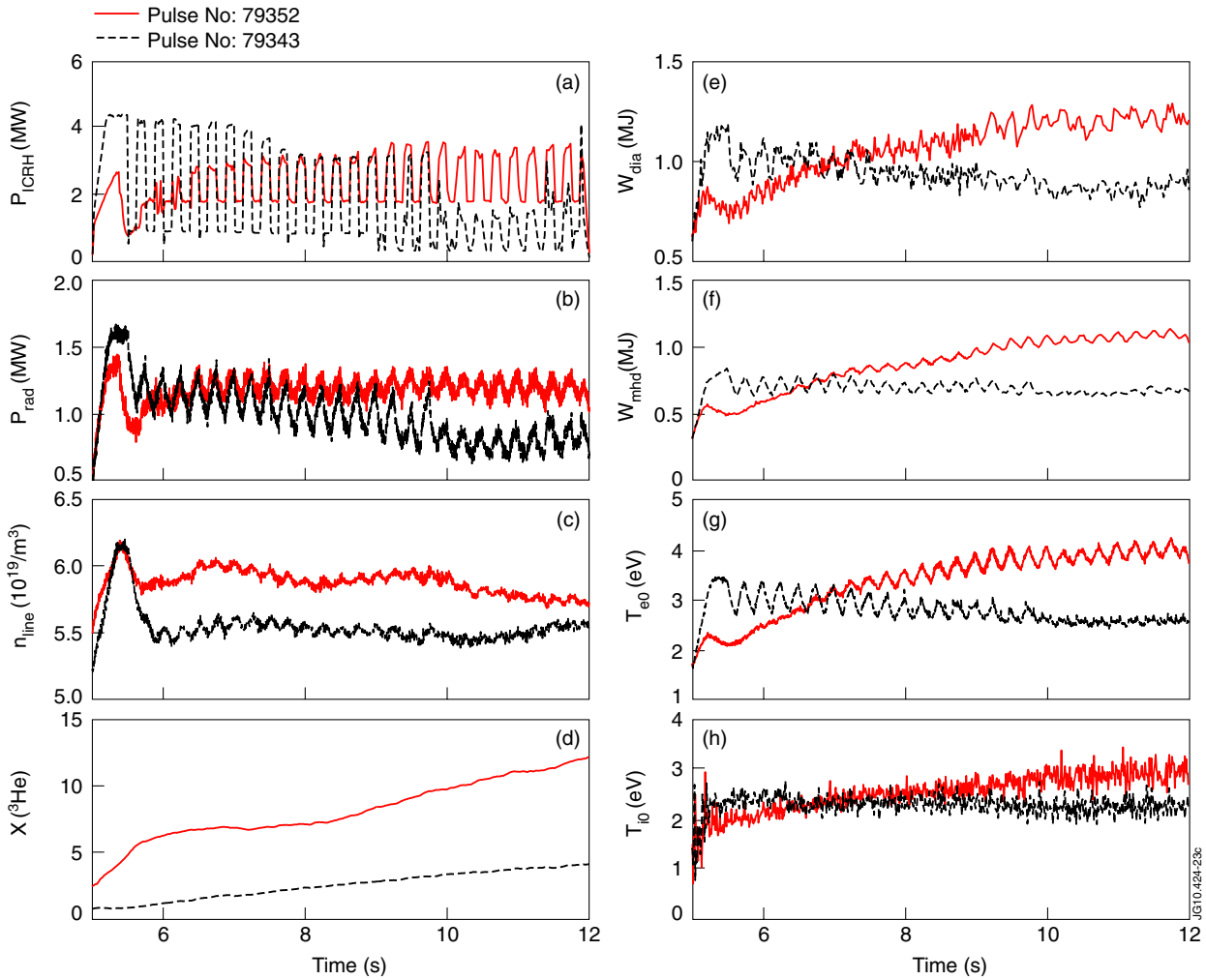

Figure 1. Overview of some characteristic quantities for shots 79343 (with a modest $X[^3\mathrm{He}]$ scan) and 79352 (in which $2.5\% < X[^3\mathrm{He}] < 12\%$): (*a*) modulated ICRH power, (*b*) radiated power, (*c*) line integrated density for a chord through the plasma center, (*d*) real time control estimate of the ^{3}He concentration, (*d*) diamagnetic energy, (*e*) plasma energy, (*g*) central electron temperature and (*h*) central ion temperature.

(figure 1(*h*)) is not easily identifiable by the naked eye. Note that the RF system struggles to couple power at the start of discharge #79352 and at the end of discharge #79343, when the ^{3}He concentration is about 5% in both shots. Also the electron temperature response to the RF modulation is correlated with the ^{3}He concentration in the same way, showing the typical periodic increase and decrease as a result of the two alternatingly applied power levels.

For the imposed ICRF power of 3–4 MW, core temperatures of 3–4 keV are reached by the electrons, and slightly lower temperatures (2–3 keV) by the ions. Except for the radiated power, all signals for shot #79352 increase for increasing ^{3}He concentration. For the temperatures it can be seen that the whole profile responds to the ^{3}He concentration (see figure 2, together with figure 1(*d*) for the $X[^3\mathrm{He}]$ reference), the electron temperature showing a general lifting of the profile, while for the ions the response is more pronounced in the center. While the temperature gradually reduces toward the edge, the density (not shown) has an edge pedestal of (1–1.5) $\times 10^{19}$ m^{-3}, and central values reaching (2–2.7) $\times 10^{19}$ m^{-3}, depending on the minority concentration and possibly the limited but finite beam fueling.

2.2. *Dependence of key quantities on $X[^3\mathrm{He}]$*

Looking in detail at the response of various signals in figure 3, one can distinguish three different regimes as a function of the ^{3}He concentration: a regime at low concentration (<1.8%) at which the RF heating is efficient, a regime at intermediate concentrations (1.8–5%) in which the RF performance is reduced, and finally a very good heating regime at ^{3}He concentrations beyond 6%. The statistical analysis of several quantities as a function of the ^{3}He concentration in the plasma as well as evidence of the presence of fast ion particles identifies the first as a minority heating scheme, and the second and third as MC schemes.

Figure 3 depicts the average values of the electron (*a*) and ion (*b*) temperature, the diamagnetic energy (*c*) and the antenna resistance (*d*) as a function of the ^{3}He minority concentration for a number of 0.2 s time intervals at similar line

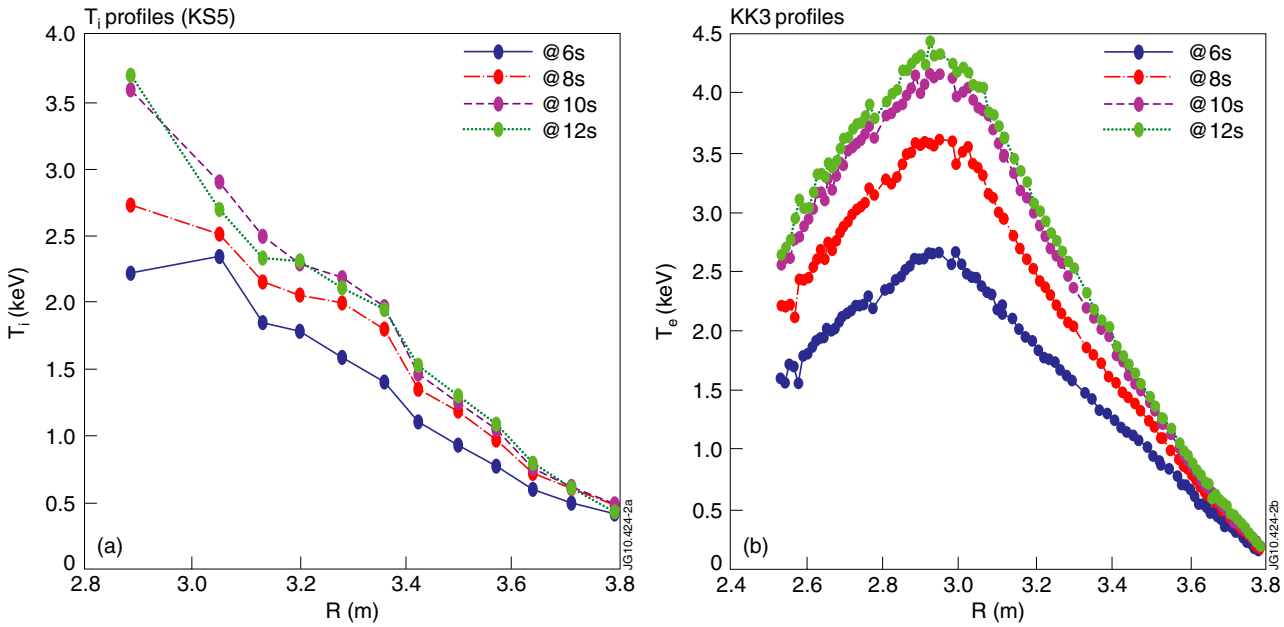

Figure 2. (*a*) Ion and (*b*) electron temperature profiles at various times and thus for various ^{3}He concentration during shot #79352 in which the minority concentration was scanned using real time controlled ^{3}He gas puffing (see figure 1).

integrated densities between 5.5 and 6×10^{19} m^{-3}. Both the diamagnetic energy and the temperature exhibit a maximum at low ^{3}He concentrations, and fall sharply in the first MC regime. Between a ^{3}He concentration of 3% and 5%, the overall performance is poor. It recovers and becomes even better than that at low concentrations in the second MC regime. Note that $T_i < T_e$, even deeply in the minority heating regime, because the ^{3}He concentration is low and the ^{3}He ions are accelerated to high energies and slow down on electrons rather on the bulk H ions. It is worthwhile to mention that the minority heating regime at low concentrations is not accompanied by a noticeable neutron yield, but that this quantity rises pronouncedly in the second MC regime (not shown). This behavior will become more clear when the fast particle content of the plasmas is discussed (see section 2.5).

The observed RF performance is not only a consequence of the wave dynamics inside the plasma but is also due to the antenna–plasma coupling. In figure 3(*d*) it can be seen that in the ^{3}He concentration intervals in which good heating efficiency is observed the antenna resistance is high, and that it disappears when approaching $X[^3\text{He}]$ of 3–6% from either side. This correlation with the concentration can directly be observed on the coupled RF power level and on the resistance of individual straps, respectively, higher and more responding to the modulation at low $X[^3\text{He}]\sim$1–2% than at intermediate concentrations of 2–4%.

2.3. Response of the plasma to RF power modulation

Studying the experimental ICRF power deposition profile is traditionally done by studying the electron and ion temperature response to a modulation of the RF power. Apart from the temperature, also other quantities such as the density and the radiated power respond to changes in the RF power level (for a detailed analysis of how these can be accounted for, see e.g. [17]). Finally, some of the power is lost before it is ever thermalized and thus the specificities of the fast particle populations (e.g. the fast ion loss) need to be monitored to obtain a full picture of the RF heating dynamics.

Figure 4 gives a typical example of the temperature response to the RF power in pulse 79352 (solid lines in figure 1). Figure 4(*b*) shows the strong electron temperature response to the ICRF power, the fast temperature increase and decrease in direct correlation with the—modulated—ICRF power level. The central ion temperature channels (figure 4(*a*)) are rather noisy but do not—at least to the naked eye—reveal any response to the RF power modulation.

A minimum of NBI power has to be applied in the shots since the ion temperature is inferred from the charge-exchange recombination diagnostic that relies on the presence of a fast ion particle subpopulation. As the temperature does not only change under the influence of the ICRF power but also under the influence of NBI power, this NBI power was kept low and constant during the shot. The electron temperature increase just after $t = 5$ s is due to the (high energy) NBI beam blip used to diagnose the plasma rotation in the MC shots. It is worthwhile mentioning that the RF generators do not succeed in modulating the power early in the discharge ($5.5 < t < 6.5$ s) and that the maximum power level launched increases as a function of time for the first few seconds after that (see figure 1(*a*)). This behavior is a consequence of the dependence on $X[^3\text{He}]$ of the efficiency with which the power can be coupled to (figure 1(*a*)) and absorbed inside the plasma.

As the electron temperature diagnostic has 96 and the ion temperature diagnostic has 12 channels covering all magnetic surfaces of the plasma, studying the response of all temperature channels to the launched RF power allows determining the experimental power deposition profile.

In figure 5(*a*) the power densities estimated from the temperature responses shown in figure 4 between 7 and 8 s

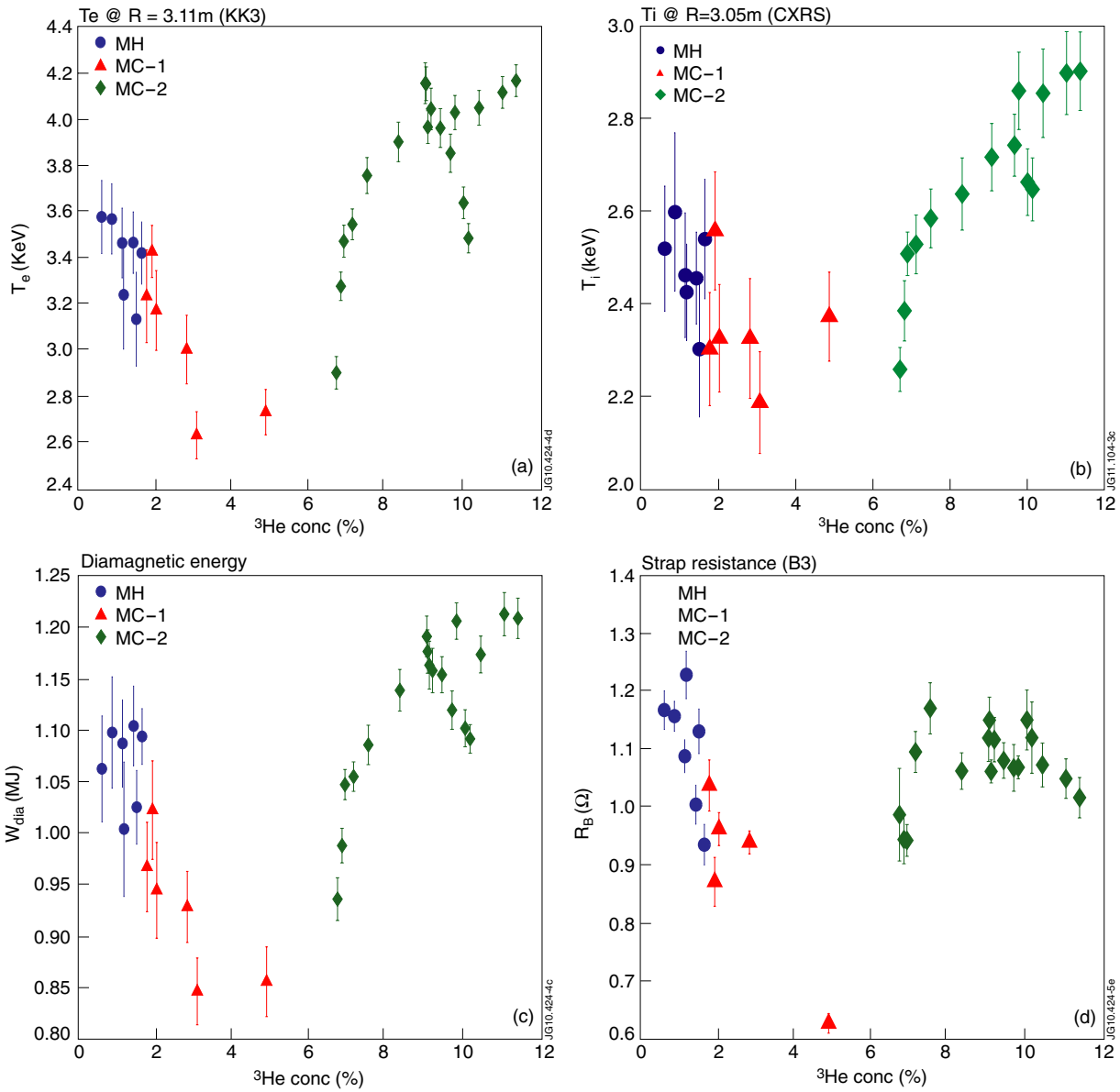

Figure 3. Summary plot over the full experimental session of various key quantities as a function of the ^{3}He concentration: (*a*) electron temperature, (*b*) ion temperature, (*c*) diamagnetic energy and (*d*) coupling resistance of antenna B. The data points represent the various quantities averaged over 0.2 s.

are depicted; the corresponding integrated power density is provided as well (figure 5(*b*)). Both the ion and electron profiles have a broad deposition profile with a maximum in the center. Electron heating is clearly more dominant than ion heating, the volume integrated electron power density being about a factor of 3–4 larger than the volume integrated ion power density; Fourier and break-in-slope analyses yield similar results.

That the ^{3}He concentration is a key parameter in the examined shots is clearly seen in figure 6. Both at low (figure 6(*a*)) and at high (figure 6(*b*)) concentration the maximum absorbed electron power density shifts outward for increasing ^{3}He concentration; the modulation frequency is 25 Hz rather than 4 Hz so the ion dynamics is not captured anymore. At low concentration the maximum moves out rapidly depending on the minority concentration (the minor radius position shifting from $\rho_{max} \sim 0.4$ m when $X[^3\text{He}] = 2.5\%$ to $\rho_{max} \sim 0.55$ m when $X[^3\text{He}] = 3.3\%$), while at higher concentrations the position of the power density maximum seems to be less affected by the ^{3}He content of the plasma. At first sight the location of the maxima seems puzzling: the fast-moving maximum seems to disappear at higher concentrations, and a new maximum enters the picture. It will be shown further on that this seeming inconsistency can be easily explained as being a result of the existence of two rather than just one MC layers appearing due to the complex composition of the plasma.

The results of the RF absorption efficiency analysis as a function of the ^{3}He concentration are summarized in figure 7. The full dots represent the absorption by the ions, electrons and the summed power obtained from analyzing the charge exchange and ECE temperature profiles. The total absorbed power efficiency obtained by performing a

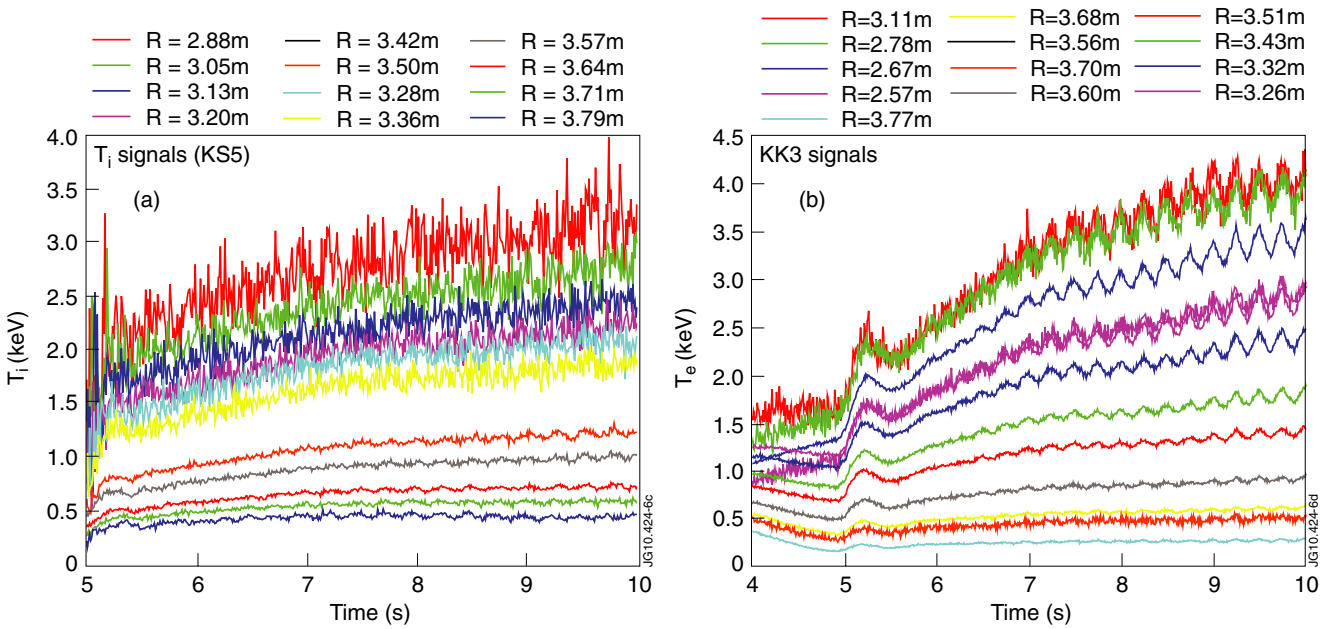

Figure 4. (*a*) Ion and (*b*) electron temperature responses to the auxiliary heating power for shot #79352 (see figure 1)

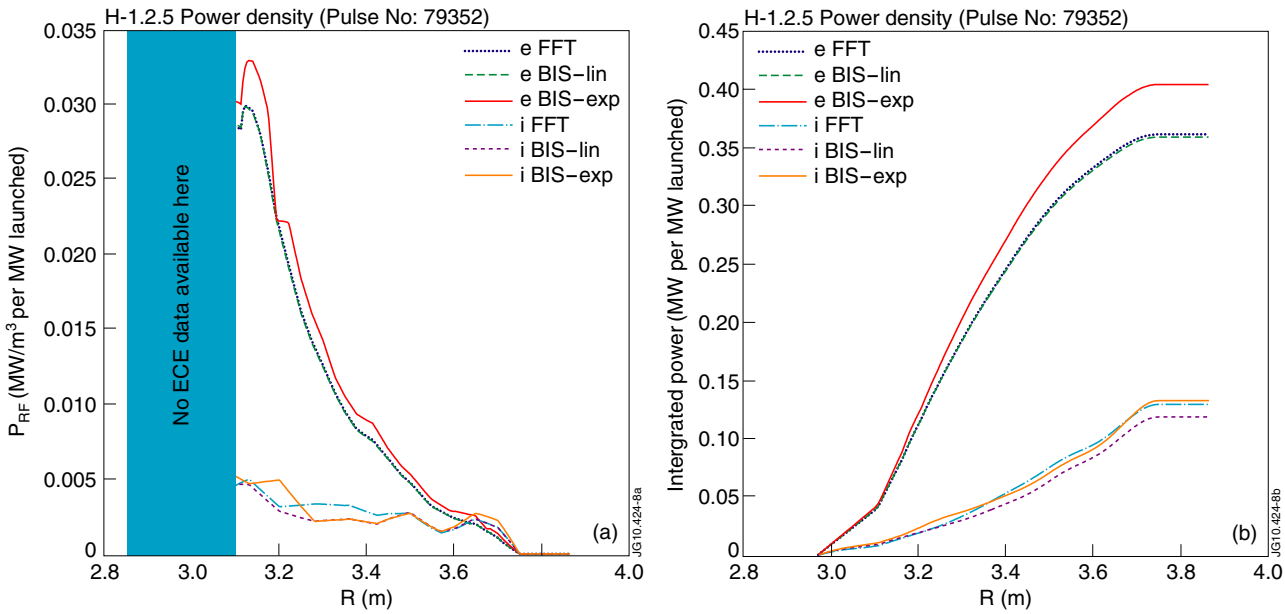

Figure 5. (*a*) electron and ion ICRF power deposition profile obtained by FFT or BIS analysis for shot #79352, and (*b*) corresponding volume integrated electron and ion power densities.

Fourier analysis on the global MHD energy is depicted as diamonds. The two are in reasonable agreement, although the heating efficiency derived from the global MHD energy tends to be somewhat higher than the heating efficiency derived using the temperature and density profiles. Taking into account that e.g. the ion temperature signal is somewhat noisy, one possible explanation is that this difference is due to the intrinsic inaccuracy of the diagnostics. The difference may, however, even more simply be due to the fact that some physics aspects are not properly included: e.g. both the reconstituted electron and ion temperature tend to be asymmetric w.r.t. the magnetic axis, suggesting that effects such as trapping of non-thermalized populations should be taken into account. The (bulk) temperatures do not account for the energy carried by fast subpopulations. Particularly at lower concentrations ($X[^3\mathrm{He}]\sim 1\%$), some of the power is expected to be carried by non-thermal ions. Globally, the absorption efficiency is 60–70% so the (^{3}He)–H plasma can be heated efficiently both in minority and MC scenarios, be it that the heating efficiency in the first MC regime is degrading. To find out if this non-wanted effect is intrinsic or can be avoided, an analysis is needed to explain exactly why this is happening. The fate of the remaining 30–40% of the wave power is outside the scope of this paper. It should be recalled, for example, that only the temperature and not the density response to changes in the RF power were accounted for

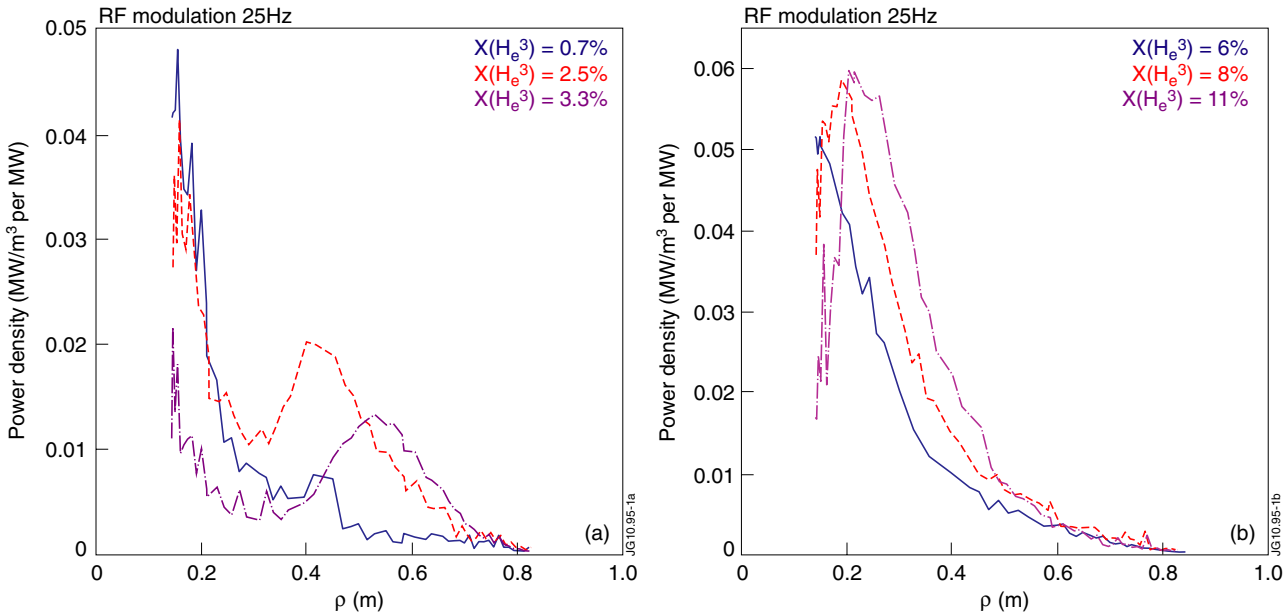

Figure 6. Electron power deposition profile for various ^{3}He concentrations inferred from analysis of the electron temperature to a 25 Hz modulation of the RF power: (*a*) $X[^3\mathrm{He}] = 0.7\%, 2.5\%, 3.3\%$, (*b*) $6\%, 8\%, 11\%$.

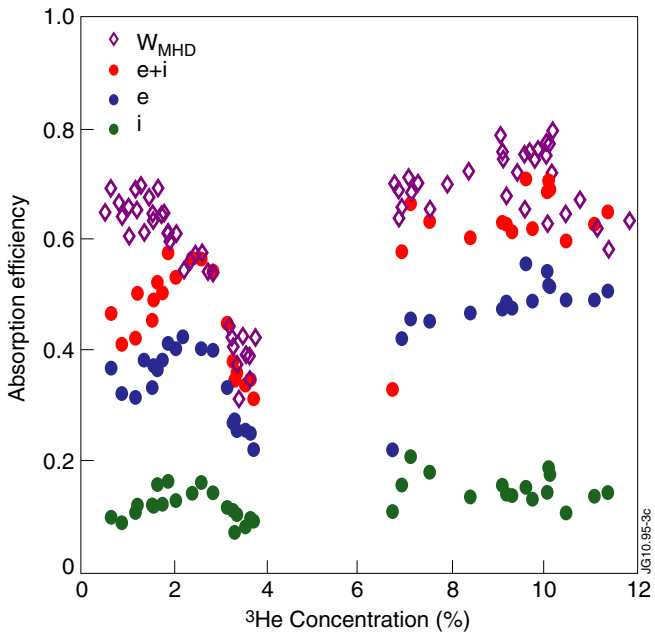

Figure 7. Summary of the absorption efficiencies as a function of the ^{3}He concentration estimate provided by the formula used to steer the real time control gas puffing.

when computing the *local* power absorption at various radial locations, while some density response to the modulation of the ICRH power can clearly be observed at low concentrations; detailed information on the local density response is not available on the same time scale as the ECE data but the observed variations of the available density channels suggest that adding the density response would add an extra 10–15%. Also the absorbed power is normalized to the launched power and not to the net power available after subtracting the impact of radiation; normalizing to the net available power would add another ∼15%. Edge effects such as collisional absorption, non-resonant absorption and recycling due to fast particles intercepting the wall are likely to be responsible for some of the absorption efficiency differences and should strictly be included to more rigorously assess the missing power (see e.g. [17]). Finally, the points plotted in figure 7 result from Fourier analysis of the temperature response to the RF power modulation. As these data is only accounting for the dominant term in the Fourier spectrum but not the full response, the data are likely to somewhat underestimate the actual heating efficiency.

As mentioned before, figure 7 reveals that there are several distinct heating regimes as a function of the ^{3}He concentration. At low ^{3}He concentration the heating efficiency inferred from the bulk species grows as a function of $X[^3\mathrm{He}]$ up to $X[^3\mathrm{He}]$∼2–2.5%; in this region the MHD energy results (diamonds) indicate a higher heating efficiency than the results derived from the detailed profile analysis. Beyond the maximum at $X[^3\mathrm{He}]$∼2%, the heating efficiency degrades quickly. In this latter region the MHD energy and detailed profile analysis results totally corroborate one another. In the $X[^3\mathrm{He}]$ region from 4% to 6%, no trustworthy data could be obtained since the ICRF generators are struggling to couple power into the plasma, rendering the efficiency analysis impossible. Noting that the antenna resistance drops down significantly in this region (see figure 4(*d*)), the reason for this 'void' is thought to be related to the changing wave propagation and/or damping as will be discussed later on in this paper. When reaching $X[^3\mathrm{He}]$>6%, the heating efficiency has fully recovered and is weakly dependent on the minority concentration.

One aspect to keep in mind when interpreting the plasma response to RF power modulation is that the temperature profile is shaped not only by the power sources but equally by the power losses. In figure 8 the power deposition

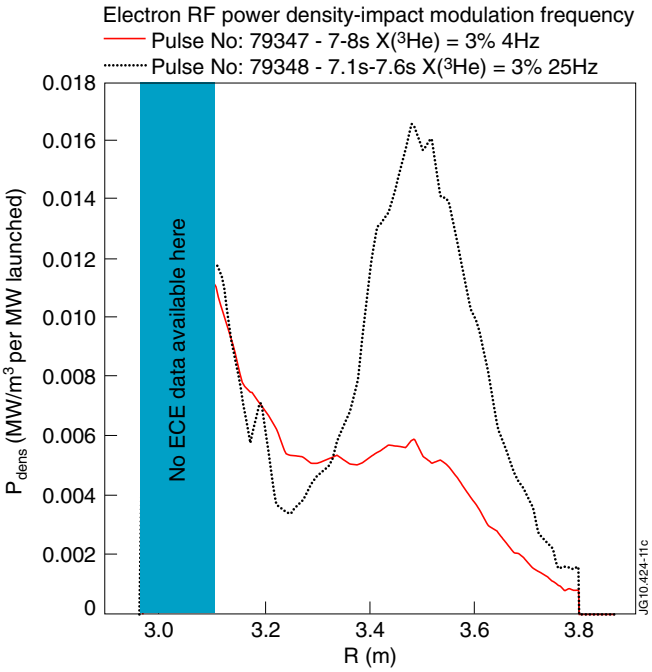

Figure 8. Electron power deposition for a given ^{3}He concentration of 3% but inferred from the electron temperature response to a 4 or 25 Hz modulation of the ICRF power launched.

profile is given for two time intervals in different shots with different modulation frequencies but with the same ^{3}He minority concentration of 3% and as identical as possible plasma and machine parameters. Both profiles exhibit a power density maximum close to the plasma core ($R \sim 3$ m), and share the same location of the power density maximum at $R \sim 3.5$ m. But in spite of the similar conditions, the two power deposition profiles are markedly different, the profile at 25 Hz being much more peaked than that at 4 Hz. The former has a power density maximum of $\sim$0.006 MW m^{-3} per MW launched while the latter's peak is almost 3 times higher. Also the integrated electron power is significantly different: for slow modulation at 4 Hz only 25% of the power is found back in the electrons, while 50% is recovered when $f_{\mathrm{mod}} = 25$ Hz. As the parameters have been chosen to be identical, the main effect that sets these two results apart is the diffusion of heat across the magnetic surfaces, and ultimately out of the plasma. When the modulation is fast, the temperature response mimics the deposition profile. But as heat diffuses away from the location where it was deposited, slow modulation tends to yield broader deposition profiles with a lower maximum than rapid modulation. Transport also carries heat across the plasma boundary causing a fraction of the power to be missing; part of the absorbed power also goes unnoticed because the line of sight of the JET ECE diagnostic is $\sim$20 cm below the actual magnetic axis, thus creating a 'hole' in the data for the plasma core. Finally—and recalling that the radiated power is a sensitive function of the ICRF power in the plasmas studied here—some of the power is radiated away from the plasma in the form of Bremsstrahlung and/or impurity radiation. As the average fraction of the power radiated away can be as high as 25–50% (see figure 1) of the applied power, the effective power available for heating the plasma is often significantly lower than the power launched. Although this realization does not make the heating scenario more efficient, it at least suggests that little power is lost to unidentified channels.

2.4. Multiple MC: sensitivity of the power density on the plasma composition

Since the position of the MC layer critically depends on the plasma composition, a real time control scheme has been implemented in JET to impose a given value for the minority concentration in the experiments. The real time control scheme relies on a simple formula to estimate the ^{3}He concentration and adopts a Proportional Integral Derivative (PID) scheme to open the gas injection module whenever the measured concentration drops below the wanted one. The ^{3}He concentration estimate is based on a formula—originally due to Mantsinen [18]—that is based on the expressions for the charge neutrality and the effective charge, and that links relative divertor light intensities of different plasma species to relative concentrations. Although this scheme is crude and incapable to make an accurate guess of the actual ^{3}He concentration in the plasma, it is sufficiently accurate to allow steering the minority gas injection module.

Because of the CFC wall tiles, JET plasmas typically contain a few per cent of carbon. Additionally, deuterons and ^{4}He ions released from the wall by recycling were present in all discharges since D is the machine's most commonly used working gas and the reported experiments were performed after a ^{4}He plasma campaign. Because of the non-availability of hydrogen beams, D beams were used instead to help diagnosing the plasma. Hence, the concentration of D ions was further enhanced. Finally, it is likely that residual NBI duct 'contamination' from the recent changeover from ^{4}He to D beams added traces of ^{4}He to the plasma.

As the location of the IIH layers critically depends on the plasma composition, experimentally found MC absorption positions can be correlated with the concentration of the different plasma species via a dispersion equation study. It was found that the presence of the non-intended small quantities of C, D and ^{4}He in the plasma—in addition to the injected ^{3}He—gave rise to a supplementary MC layer close to the plasma center. Recall that the ECE diagnostic at JET has a line of sight that is $\sim$0.2 m under the actual magnetic axis and thus the electron RF power density very close to the magnetic axis cannot be experimentally studied. The rise toward the axis of the electron power density inferred from the ECE data at low $X[^3\mathrm{He}]$ in figure 6 can thus be attributed to this second conversion, although the actual maximum is not clearly seen until the ^{3}He concentration is $\sim$8%. Because of the large uncertainties inherent to the procedure used to calculate the ^{3}He concentration and because of the unknown level of ^{4}He in the plasma, a minimization was performed to estimate the actual plasma composition consistent with the experimentally determined power deposition data. The various plasma concentrations were taken as free parameters in the minimization. Starting from an initial guess for the plasma composition, the experimentally found MC positions (up to a small shift with respect to the position of the

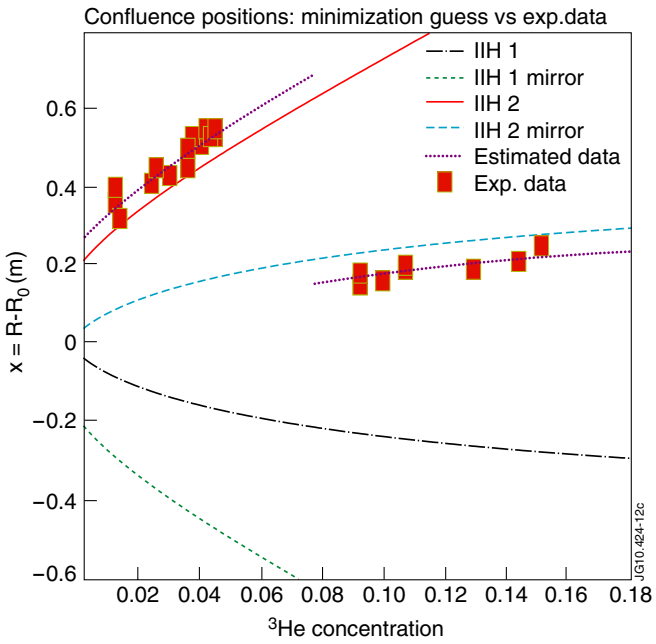

Figure 9. Result of the minimization procedure adjusting the plasma composition to get a dispersion equation fit of the experimental positions (squares) of the confluence region position as a function of the ^{3}He concentration guess provided by the real time control formula.

FW confluence because the damping on the mode converted branch only becomes efficient a small distance away from the confluence after the wave has modified its $\boldsymbol{k}$-vector sufficiently to guarantee efficient damping) were identified with the IIH locations provided by a cold plasma dispersion equation root finder. This minimization analysis allows us to state more firmly that the central maximum in absorption in figure 6(a) is due to MC and not simply due to FW electron damping.

As all D-like species play a similar role from the ICRF heating point of view (the cyclotron frequency being proportional to Z/A), it is difficult to discriminate between the various D-like components in the proposed procedure. Although the average experimental curves could easily be identified with the corresponding confluence positions, the slope of the experimental data as a function of the ^{3}He concentration could not be matched, while the required D-like concentrations seemed excessive and outside the physically acceptable range. Realizing that the ^{3}He concentration used here as a reference is the guess obtained from the real time control formula (lacking e.g. profile information), it seemed plausible that a corrective factor should be applied to link the estimated ^{3}He concentration with the one at the MC layer. A multiplicative correction factor of 1.6 is found via the minimization. The corresponding confluence layer position data for experimental and guessed concentrations are given in figure 9; since some of the MC layers are on the HFS but as the break-in-slope and Fourier analysis is performed on the LFS temperature data, their mirror position with respect to the magnetic axis—roughly identifying the same magnetic surface—is also plotted. The obtained multiplicative factor corrects for the fact that the light intensity is not only a function of the concentration of the examined species but equally of the ambient temperature and electron density. Furthermore, one of the signals used for computing the real time control guess of the ^{3}He concentration is the relative light intensity of hydrogen and its isotopes. Whereas the error in X[H]/(X[H]+X[D]) is typically small (of the order of a few per cent) in D majority plasmas, the error on X[D]/(X[H]+X[D])—H rather than D now being the majority gas—is much bigger. Preliminary charge-exchange recombination spectroscopy data of the ^{3}He profile provide a similar correction. Finally, the TOFOR neutron diagnostic provides a rough guess for the actual D-concentration by comparing the ratio of the beam-thermal and beam–beam neutron emission [19]. A value of X[D]∼5–7% found is in good agreement with the guess provided by the minimization analysis and by spectroscopic measurements.

2.5. *RF induced fast particle populations*

Many ion heating scenarios are based on the capacity of ICRF waves to accelerate ions to high energies and deform the particle distributions well away from that of a thermalized population. JET has a number of diagnostics that allow monitoring the fast particles, either directly (as is the case for the fast lost ion collector [20] and neutral particle analyzer [21]) or indirectly (as is the case for the gamma ray spectrometers [20] or the time-of-flight neutron diagnostic [22]).

A first hint that fast particles were created in the (^{3}He)–H MC experiments is given in figure 10. In the top right figure the neutron rate is depicted for two shots, shot #79347 with a ^{3}He concentration scan at modest concentrations and shot #79349 with ^{3}He concentrations increasing from ∼2.5% and to ∼12.5% (see figure 10(b)). Although the average ICRF power level is lower for most of the time in the discharge with the highest X[^{3}He], the relative neutron rate is significantly different. Both neutron rate curves show a very similar behavior early in the shot (including the response to the already mentioned initial 130 keV NBI blip) when their ^{3}He concentrations are similar but diverge gradually more as the difference in the ^{3}He concentrations become larger. The signature of the ICRF modulation is evident in the high concentration shot but is totally absent in the low concentration one. The already discussed correlation between the coupled power and the ^{3}He concentration is noticeable here as well: when X[^{3}He] is about 3%, the maximum of the launched wave power is ∼4 MW, but when the concentration rises further to ∼4%, there is a strong decrease in the maximal power launched.

Apart from the neutron rate, gamma ray spectroscopy (with both vertical and horizontal spectrometers) shows a very different pattern for these two shots: whereas in shot #79347 no high energy gamma rays are observed, two peaks stand out distinctly in the spectrum of shot # 79352. The two maxima are the signature of threshold nuclear reactions necessitating the presence of fast ions for their occurrence. The peak at 4.4 MeV corresponds to the ^{9}Be(α,nγ)^{11}B reaction and telltales the presence of a highly energetic ($E > 1.5$ MeV) ^{4}He (α) subpopulation, while the peak at 3.1 MeV is due to the ^{12}C(D,pγ)^{13}C reaction which requires fast D ions of at least 0.5 MeV. The origin of the fast ^{4}He ions is likely not

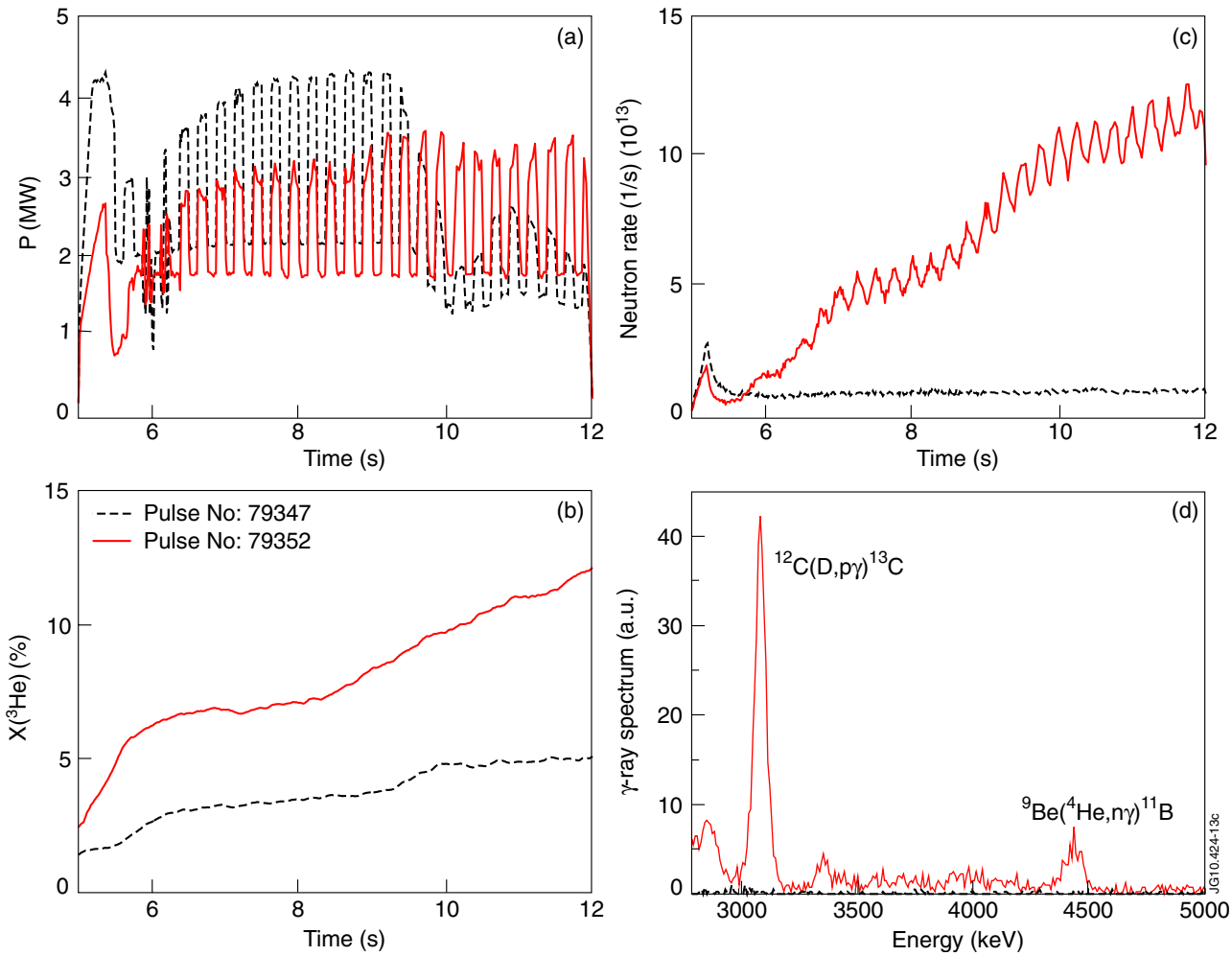

Figure 10. Evidence of ICRF accelerated fast ions, comparison of shots 79347 and 79352: (*a*) ICRF power level, (*b*) real time control ^{3}He concentration estimate, (*c*) neutron rate, (*d*) gamma ray spectra (dN/dE as a function of the energy E).

directly RF related, i.e. they are not thought to be RF heated ^{4}He ions recycled from the wall. Rather, moderately fast RF heated D beam ions colliding with ^{3}He trigger the D(^{3}He,p)^{4}He reaction forming 3.6 MeV α-particles and 15 MeV protons; in the range of effective (D) temperatures of 200–400 keV, this reaction has a cross-section that is about 4 times higher than that of the D(D,n)^{3}He reaction. The fact that reasonably fast D is present is also inferred from evidence that the D(^{3}He,γ)^{5}Li branching reaction is taking place at high ^{3}He concentrations: this reaction gives rise to a broad spectrum of gamma rays with energies between 11 and 17 MeV (not shown); for more details both on the fast ^{3}He as on the fast D and ^{4}He subpopulations in the presently studied scenario, see [20].

At very low ^{3}He concentration, the fast ion loss detector observes very energetic ^{3}He ions (see further). Whereas such a population could somehow be expected in a scenario tuned to central minority ^{3}He fundamental cyclotron ICRF heating, the D peak at higher ^{3}He concentrations is more surprising at first sight as one expects MC heating rather than ion heating to be the dominant wave energy absorption channel. Similar evidence was, however, already presented in (^{3}He)–D plasmas equally tuned to ^{3}He $N = 1$ heating but in which the NBI D beam was observed to absorb a non-negligible fraction of the RF power at the Doppler-shifted D cyclotron layer [11]. Whereas the exact role of the bulk deuterons was not fully evident in the (^{3}He)–D experiments, the present (^{3}He)–H experiments make it clear—no dominant fraction of thermal D being present in this H-majority plasma—that the earlier observed phenomena are indeed exclusively due to the D *beam* ions. Also in the recent experiments a sufficiently *large* ^{3}He concentration was the key to triggering the formation of an ICRF heated D population. Figure 11 shows the neutron spectrum provided by the TOFOR (time-of-flight) detector: whereas at modest X[^{3}He] no fast D tail is observed, a D tail with an estimated effective temperature of 250 keV was present in high X[^{3}He] shots; as TOFOR relies on the time it takes secondary neutrons to travel between two diagnostic plates the independent variable in the plot is the time of flight, which is inversely proportional to the velocity of the particle so that the signature of high energy tail is visible in the left of the figure. The neutrons TOFOR detects arise from the DD nuclear reaction. Where D was the majority plasma in the earlier (^{3}He)–D experiments so that beam–target DD reactions were abundant, D is a minority in the present (^{3}He)–H plasmas so beam–beam reactions dominate the neutron spectrum.

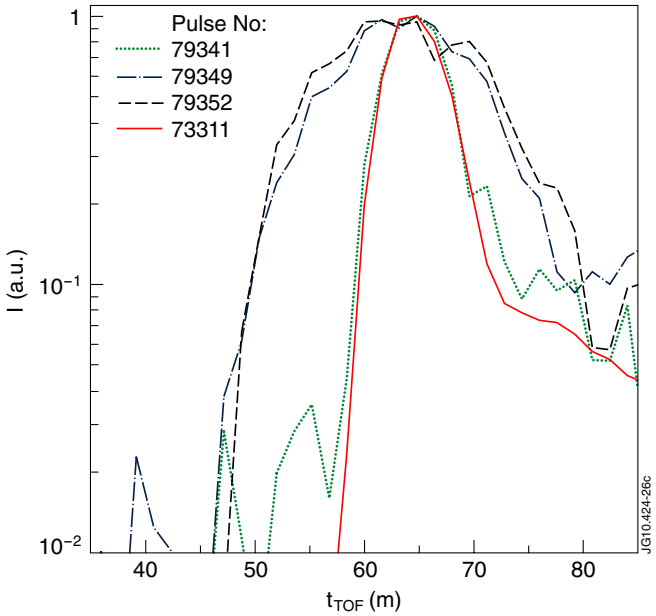

Figure 11. Evidence of ICRF accelerated fast D ions: TOFOR neutron time of flight spectrum for various shots of the (^{3}He)–H minority to MC heating session (low $X[^3\text{He}]$: #79341; high $X[^3\text{He}]$: #79349 and 79352), and for a non-ICRF-heated reference shot (#73311).

JET is equipped with a scintillator probe fast ion loss detector [20], which detects ions with gyroradii from 0.03 up to 0.14 m, and equally determines the particles' pitch angle. Fast ^{3}He ions with energies of 1.1 MeV at a pitch angle of about 70° were observed in the shots with finite but small ^{3}He content (see figure 12). Tracing back the orbits of these particles to where they obtained their acceleration places them just off the ^{3}He resonance, identifying them as trapped particles with an essentially tangent resonance (not shown). The losses diminish when $X[^3\text{He}]$ goes beyond 2.5%. There is a clear correlation between the gamma ray spectrum and the fast ion loss detector signal: in the absence of fast ^{3}He or D ions in shot # 79347, the 4.4 MeV peak in the γ-ray spectrum disappears and only the 3.1 MeV peak survives.

The scintillator probe equally detected fast D and ^{4}He particles. In shot # 79349 in which the ^{3}He concentration was about 10%, 1.1 MeV D and 2.1 MeV ^{4}He were observed early in the discharge while energies up to 1.8 MeV for D and 3.9 MeV for ^{4}He were reached later on. The pitch angle of the fast D and ^{4}He was about 57°. In shot 79352, RF modulation was used throughout the flat top and a ^{3}He concentration scan from 2% to 12% was performed. The modulation of the RF power can clearly be seen in the fast D and ^{4}He particles losses when $X[^3\text{He}]>6\%$. A loss in RF power is also immediately detected via a drop in the γ-ray signal.

2.6. A short note on intrinsic and RF induced rotation

As mentioned at the outset, the rotation analysis was done using dedicated shots designed to keep the external NBI momentum input as small as possible. Although rotation analysis is not the main topic of this paper, some relevant results of these experiments are briefly sketched here. For more information on the rotation experiments, in particular on the impact on the rotation profile and the peak rotation achieved of the heating scenario and the RF power coupled but equally of the magnetic configuration, the temperature and the density apart from the role of the ^{3}He minority concentration addressed in this paper, see [23]. Poloidal and toroidal plasma flow is typically observed via charge-exchange analysis. As charge-exchange relies on a fast ion (beam) population, the analysis of the rotation is somewhat delicate as the diagnostic beam itself transfers its momentum to the plasma and causes it to rotate. On the other hand, waiting some time after the beam switch-on is needed to ensure that a sufficient amount of charge-exchange events occur and that the required equilibration has set in. The former reason is responsible for the fact that rotation analysis is done using beam blips (in the present case of 100 ms, data being taken every 10 ms) rather than sustained beam injection. The latter necessitates discarding the first data point during each NBI blip in the analysis. The results shown are the average of the 2nd, 3rd and 4th data point after the switch-on of the diagnostic beam; various beam blips are spread over the discharge. To have an idea of the electron power deposition profile, 25 Hz modulation intervals are interspersed in between the diagnostic beam blips.

Figure 13 shows the toroidal (a) and poloidal (b) rotation profiles observed for several values of $X[^3\text{He}]$. In the absence of RF heating as well as at low ^{3}He concentration, the plasma column is co-rotating toroidally. Increasing the ^{3}He concentration results in a central counter-rotating flow. Unlike previous RF experiments done in ^{3}He–D plasmas [24], where only a central increase in the RF induced counter-rotation was observed, the whole toroidal rotation profile seems to be shifted in this case, as can be seen from the reduction in co-rotation of the outer plasma region. This difference is believed to be related to the two MC layers present in the here reported ^{3}He–H experiments (at low $X[^3\text{He}]$ one layer being on-axis and the other off-axis on the LFS). The highest counter-rotation velocities are observed at the highest ^{3}He concentrations. Central counter-rotation values of up to 6 krad s^{-1} are reached. Together with toroidal rotation, increased poloidal rotation is observed. Similar to the toroidal rotation, the poloidal rotation increases at higher ^{3}He concentration reaching up to 10 km s^{-1} in the central region of the plasma at $X[^3\text{He}] = 7\%$.

Figure 14 depicts the averaged toroidal (a) and poloidal (b) rotation per MW launched in the plasma core and near the plasma edge as a function of the ^{3}He concentration. Whereas the edge toroidal rotation simply decreases linearly with the ^{3}He concentration, the magnitude of the central toroidal rotation seems to exhibit a maximum at about $X[^3\text{He}] = 4\%$ and a minimum at 7%. At the highest concentration reached in the experiments ($X[^3\text{He}] = 12\%$) the rotation velocity is about 8 krad s^{-1}. The dependence of the rotation velocity on the minority concentration is somewhat ambiguous in figure 14 since the ICRF power level was not identical throughout the scan. Although we have shown that this is indirectly a consequence of the minority concentration as well, renormalizing the data by the relevant ICRF power level is not yielding a truly representative answer since the rotation is composed of an intrinsic component and an ICRF induced

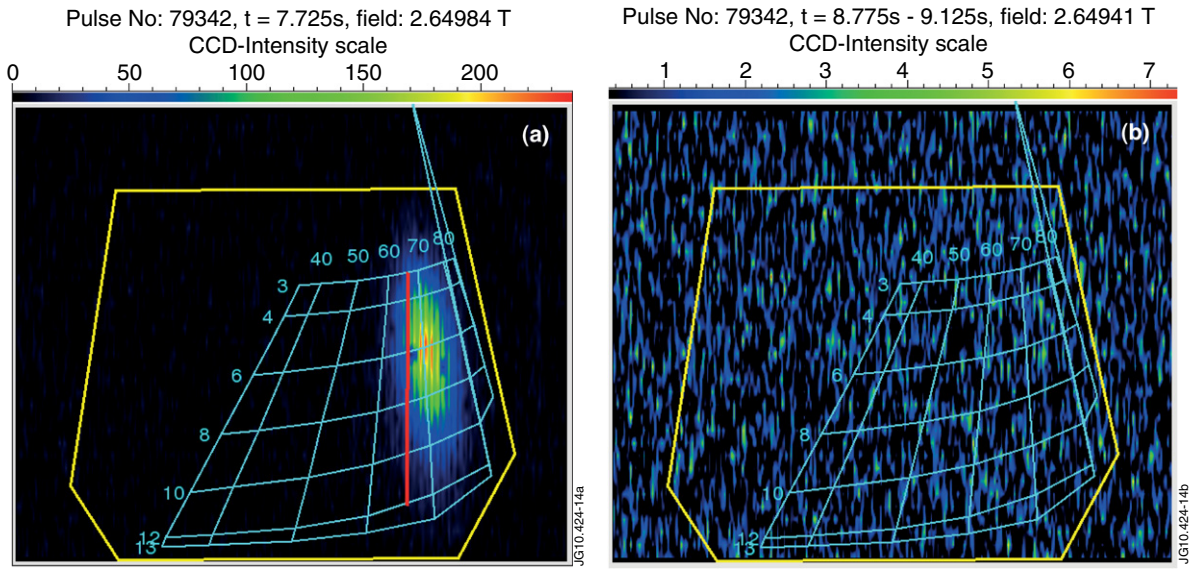

Figure 12. Lost ion detector signal for shot 79342 (*a*) at full ICRF power (3.9 MW) and (*b*) during the 25 Hz modulation phase resulting in an effective ICRF power of ∼2 MW. The ^{3}He concentrations are different but similar: 2.0% and 2.5%, respectively. The red line is the location of the ^{3}He non-Doppler-shifted resonance.

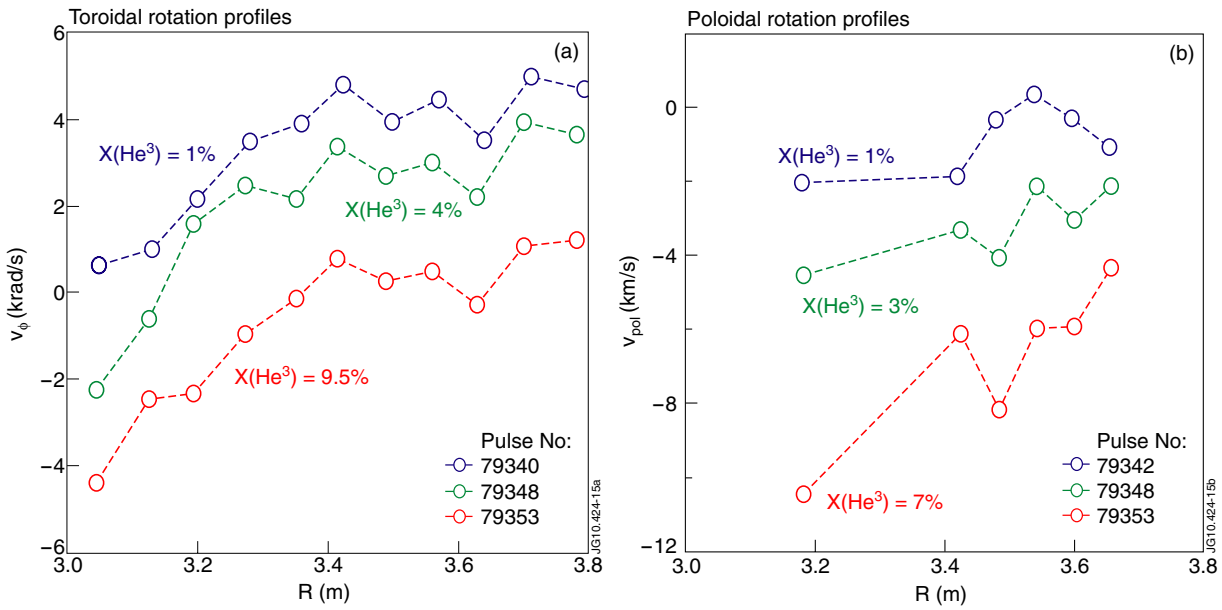

Figure 13. (*a*) Toroidal and (*b*) poloidal plasma rotation profiles measured by charge-exchange in discharges with different ^{3}He concentrations.

one so ideally one would need to subtract the intrinsic part and renormalize the RF induced part only to have an idea of the amount of rotation driven by each MW of ICRF power. But as the data of the intrinsic rotation at the temperature and density reached for each ^{3}He concentration are not known, it is impossible to disentangle the two effects.

3. Modeling

Since the short wavelength ion Bernstein or ion cyclotron branch is excited by the FW in virtually all ICRF heating scenarios—more or less efficiently depending on the parameters chosen—and since the MC layer lies very close to the ion cyclotron layer so that it is not always possible to disentangle conversion and damping dynamics, the study of the physics of MC is crucial to get a good grip on the interplay between the waves and the way their cross-talk can be enhanced or avoided. Whereas most works focus on the derivation and exploitation of an as complete as possible model (see e.g. [25–29]) and therefore necessarily rely on numerical results, it is interesting to take a step back and try to understand the basics of wave confluence using a *purely analytical* description. Obviously lacking some details and thus inappropriate to make actual predictions, such description nevertheless helps building the intuition needed to understand the observed wave dynamics.

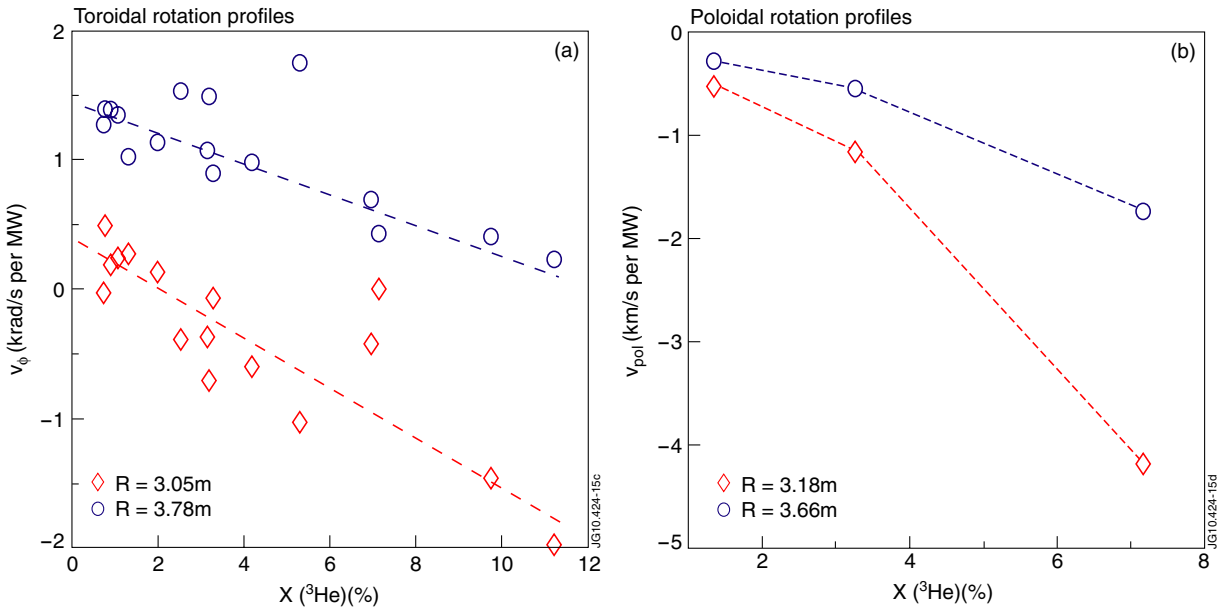

Figure 14. Dependence on the ^{3}He concentration of the (*a*) toroidal and (*b*) poloidal rotation values near the plasma center and near the edge.

In view of the vastly different wavelengths of the waves involved, the essence of FW MC near the IIH layer is captured by Budden's equation [30] which retains the FW cutoff close to the confluence but replaces the shorter wavelength branch by a resonance. Up to small corrections, the connection coefficients of the Budden equation agree with those of the longer wavelength mode incident on the confluence from the LFS in the more sophisticated tunneling equation (see e.g. [31, 32]), the latter equation modeling both interacting waves rather than just retaining the longer wavelength one. Using asymptotic techniques, it can analytically be shown that the power fraction P_{MC} lost from the incident wave to the shorter wavelength branch at the confluence is $P_{MC} = T(1 - T)$, with T the power transmission coefficient. An intuitive 'in the absence of damping, whatever is lost from an incident wave has to be transferred to the other wave' reasoning tracing the fate of the wave power through a black box that is set over the confluence shows that this mathematical relation can be understood in a very intuitive way. Whereas the Budden and the tunneling equations allow us to understand what happens at an isolated confluence, Fuchs [33] argued that the FW excited at the LFS generally proceeds to its HFS cutoff in the low density region after it has gone through the MC region where it locally excited a short wavelength branch. Hence a finite amount of wave energy is re-incident on the conversion region, this time from the HFS. The interference between the primary and re-incident waves is outside the scope of Budden and tunneling equations. Fuchs analytically determined the connection coefficients for that more general situation. He found that the same 'black box' reasoning can be used to predict the generalized connection coefficients provided that one ingredient is added to it: the evolution of the wave phase needs to be properly tracked in the case of multiple incidences of a wave on the same conversion layer. Whereas straightforwardly re-applying the 'black box' reasoning for the second encounter one would find that the total MC power connection coefficient resulting from the two encounters is simply doubled, the more rigorous result turns out to be $2T(1 - T)(1 + \sin\alpha)$ where $\alpha = 2\Phi + \Psi$ is the phase of the total reflected wave with Φ the wave phase difference between the confluence point and the HFS cutoff, and Ψ the phase of the reflected wave on the LFS. Note that the MC coefficient can now reach any value between 0 and 1 provided the parameters are chosen such that T reaches its maximal value, 1/2. Tuning the plasma parameters appropriately thus allows a significant increase in the energy ultimately damped on the short wavelength branches. Kazakov [34] studied the case of a double MC layer, the situation encountered experimentally at low $X[^3\text{He}]$. Relying on the phase integral method he found that the total MC coefficient for a wave incident on a double confluence layer is $T_1T_2(1 - T_1T_2) + 4T_2(1 - T_2)(1 - T_1)\sin^2\alpha/2$ in which T_1 and T_2 are the transmission coefficients through the individual evanescence layers and located closer to the HFS and LFSs, respectively. The interference term involving the angle $\alpha = 2\Phi + \Psi_2 - \Psi_1$ sensitively depends on the distance between the conversion layers. Including both confluences and the HFS cutoff, he further generalized the MC connection coefficient, which then has three oscillating contributions due to the interference of the incoming wave with the waves reflected from the various cutoffs [35].

Both the Fuchs and Kazakov expressions show that the constructive/destructive interference of the various waves critically depends on the relative position of the various confluence and cutoff layers. For the case of Alfvén heating this effect was noted by Karney *et al* [35]. A similar effect—upon accounting for the wave reflection from the metallic wall of the vessel—was found by Heikkinen *et al* [25]. More generally, Monakhov [13] included the layer surrounding the plasma in his description and thus described the wave interference in a global plasma + vacuum cavity.

The earlier mentioned analytical expressions show that the study of the roots of the dispersion equation permits to assess

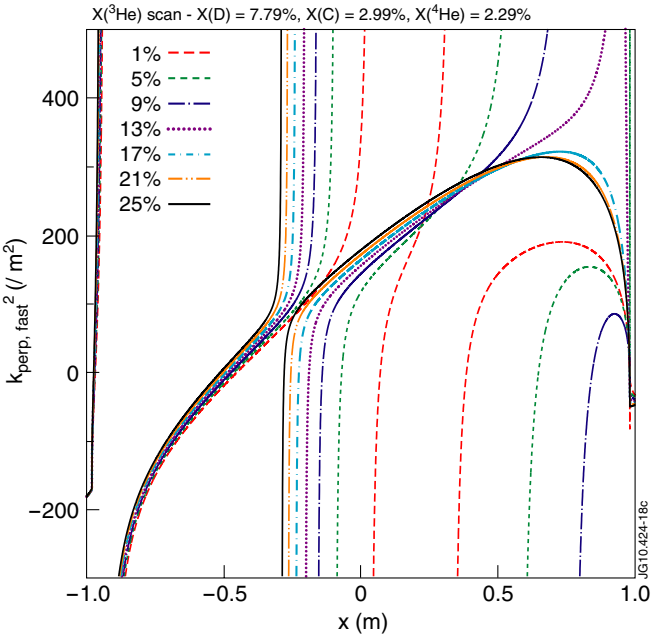

Figure 15. Cold FW dispersion equation roots for various ^{3}He concentrations.

the tunability of the MC scheme in a simple way: if cutoff and confluence positions are sufficiently sensitive functions of tunable parameters (such as e.g. the density, the minority concentration, the main modes in the antenna spectrum or the magnetic field) constructive interference can actively be maximized. As the ICRF power is mainly carried into the plasma by the fast magneto-sonic wave, this root will be studied next.

Figure 15 represents a typical FW dispersion for the recent (^{3}He)–H experiments in JET. The magnetic field and frequency considered are $B_o = 3.41$ T and $f = 32.35$ MHz, placing the ^{3}He cyclotron layer slightly on the LFS of the magnetic axis. The sensitivity of the LFS conversion/cutoff layer position to $X[^3\text{He}]$ is clear when looking at the figure: A 4% change in $X[^3\text{He}]$ results in a 0.2 m change in the cutoff position; the HFS MC position is less sensitive. Particles with the same Z/A as D (C, ^{4}He) equally have an impact on the position of the confluence layer and hence on the deposition profile (not shown). For each 5% increase in the concentration of the species with D-like Z/A the FW cutoff moves ∼0.1 m toward the LFS edge. Apart from the effect they have on the position of the conversion layer close to the antenna, the D-like species affect the wave fate in another important way by introducing a supplementary conversion layer. Just like the ^{3}He minority ions, the D ions form an inverted scenario population with the majority H, this second confluence layer shifts toward the HFS for increasing $X[^3\text{He}]$ at constant concentration of the D-like species, i.e. toward the LFS for fixed $X[^3\text{He}]$ and increasing X[D]. The position of this layer is less sensitive to the ^{3}He changes than the one first discussed. Also the HFS cutoff ($X \sim -0.5$ m) is hardly budging when the concentrations are varied.

On the other hand, the high field cutoff position is a very sensitive function of the local parallel wave number: e.g. changing the toroidal mode number from 25 to 30 moves this cutoff by 0.2 m (not shown). The LFS and inner cutoffs are, in turn, much less sensitive to this parameter. And as the FW cutoff position in the low density region is not only a function of the edge density but also of the parallel wave number, one can easily show that the density profile factor as well as the edge density have a big impact on the position of the FW cutoffs.

The TOMCAT 1D wave equation code [29] has been used to analyze the wave propagation and damping dynamics of the (^{3}He)–H scenario somewhat more quantitatively.

Figure 16(*a*) shows the localized electron deposition profiles consistent with the two confluence layers, figure 16(*b*) depicts the dispersion equation roots and figure 16(*c*) gives the corresponding parallel electric field component responsible for electron Landau damping. The ^{3}He cyclotron damping is taking place at $x \sim 0.2$ m but the ion heating is completely dwarfed by the electron heating. Short wavelength structure locally strongly enhances the electron damping (the net electron absorption being proportional to the perpendicular wave number squared) while the ion heating is inefficient as the component responsible for ion heating is small near the cyclotron layer but large near the confluence layers which are well separated from the Doppler widened region where cyclotron interaction would be possible.

The heating efficiency for a number of toroidal mode numbers as computed by TOMCAT is shown in figure 17. Experimentally observed densities and temperatures are used and it is assumed that the earlier discussed D, ^{4}He and C concentration estimates are accurate. The mode numbers chosen are representative for the main lobe of the vacuum dipole antenna phasing spectrum; the deformation of the antenna spectrum between the launcher and the antenna has not been accounted for. The oscillating character of the heating efficiency as a function of the minority concentration is the consequence of the constructive and destructive interference discussed by Fuchs and by Kazakov. Minority heating is significant only at very low ^{3}He concentrations while electron heating dominates the overall absorption. Depending on the antenna phasing chosen the cumulative effect of the various toroidal modes is different. Adding several modes tends to smoothen out the oscillations at the modest concentrations. Since the heating efficiency of all the toroidal modes degrades when approaching the $X[^3\text{He}] = 4\%$, one expects a marked decrease in heating efficiency when approaching that concentration independent of which phasing is chosen. At high $X[^3\text{He}]$ the heating efficiency is markedly less dependent on the actual value of the concentration than it was at the lower concentrations but strongly depends on the toroidal mode chosen. In between these two distinct regions there is a gap: Just like the coupling is poor in that $X[^3\text{He}]$ range in the experiment, the wave model suffers from the proximity near the LFS edge of a confluence and cutoff, preventing the power to reach the plasma core.

Qualitatively, the two types of behavior, as well as the changeover, are explained using the Fuchs conversion efficiency expression and the extension of it provided by Kazakov: The sensitivity due to the constructive/destructive interference caused by the presence of the multiple conversion layers and the FW cutoffs, the inability to couple power

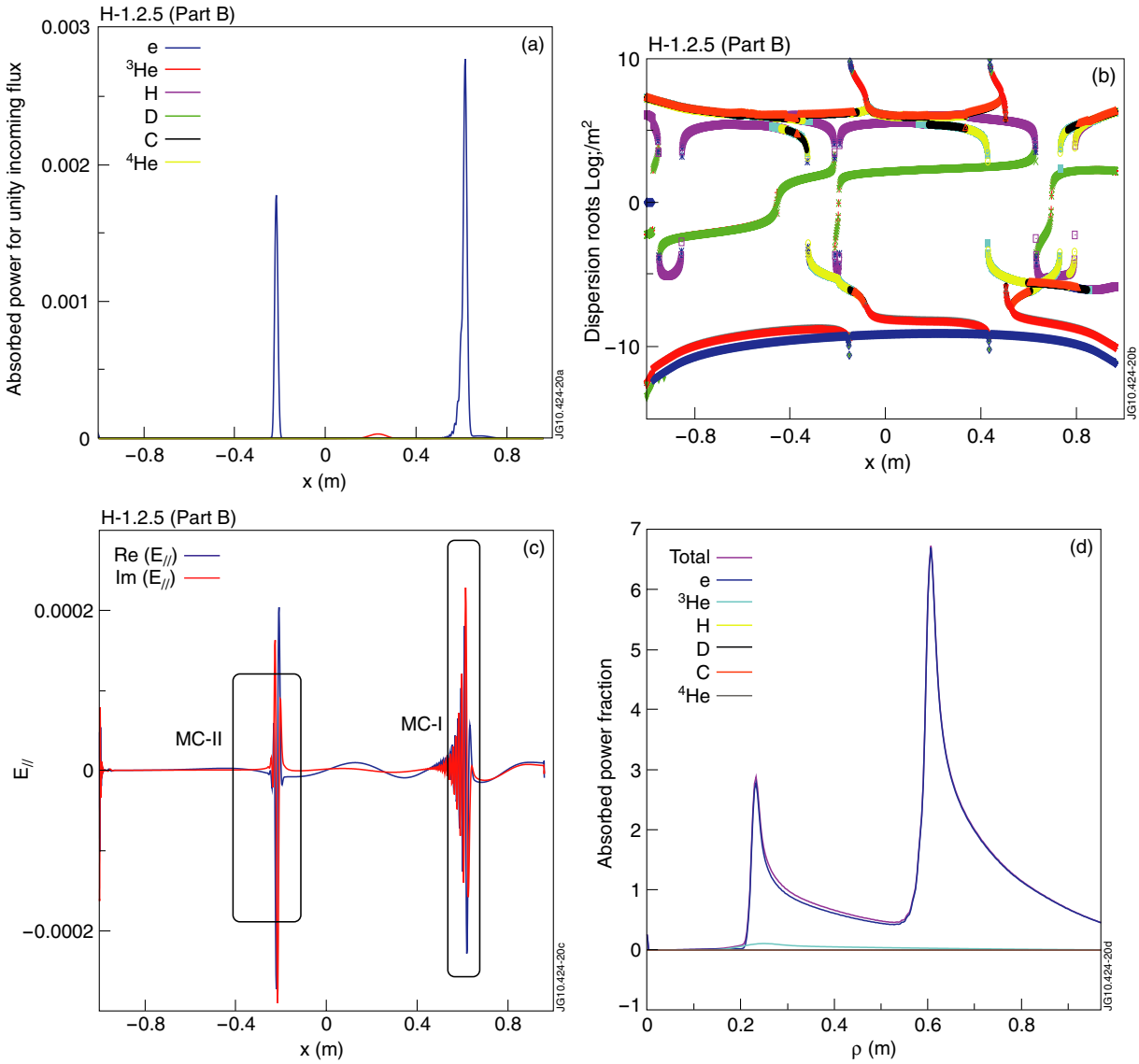

Figure 16. (*a*) Power deposition profile, (*b*) dispersion equation roots and (*c*) parallel electric field for a typical 2-MC layer MC heating scenario. Subfigure (*d*) shows the deposition profile as a function of the flux surface labeling factor ρ applying a '2D mock-up'.

efficiently when a conversion layer blocks the waves penetrating the plasma, and the soothing effect of one of the conversion layers no longer lying in the plasma.

It goes without saying that the simple 1D analysis adopted in the present section cannot give a full grasp of the *fate* of the mode converted branch, in particular the interplay between temperature and poloidal field effects that reign the competition that decides on whether the backward Bernstein or the forward ion cyclotron wave ultimately carries the wave power away from the confluence region [37]. A distinction needs to be made, however, between the actual linear MC process itself (occurring where the two interacting waves locally have matching $k_\perp^2$ and polarizations) and what happens to the excited short wavelength mode *away* from the conversion layer (when its $k_\perp^2$ significantly exceeds that of the FW). Whereas first and second order finite Larmor radius terms merely add corrections to the physics of what happens *close to* the MC layer in the type of plasmas considered in this paper (for which the relevant conversion layers are already present in the cold plasma description and a simple model suffices to localize these layers and to give a fair first assessment of the conversion efficiency), the combination of finite Larmor radius and poloidal field effects is crucial in determining the fate of the latter converted wave when it propagates *away* from the FW MC layer. Being a 1D wave code and thus by definition lacking 2D effects such as wave focusing, and missing a proper global description of the real geometry, TOMCAT's estimates thus need to be supplemented with those of a 2D wave code. Figure 18 depicts the deposition profiles computed by the TORIC wave code [28] and overlays them with the experimental deposition profiles. Realizing that the experimental deposition profiles do not discriminate between heat directly absorbed by waves on a given magnetic surface and heat indirectly ending up on the electrons either via transport in physical space or by Coulomb relaxation of an energetic (D or ^{3}He) tail onto the electrons, a fair agreement between experimental and predicted data is obtained. The 2D deposition profiles are broader than their 1D equivalents

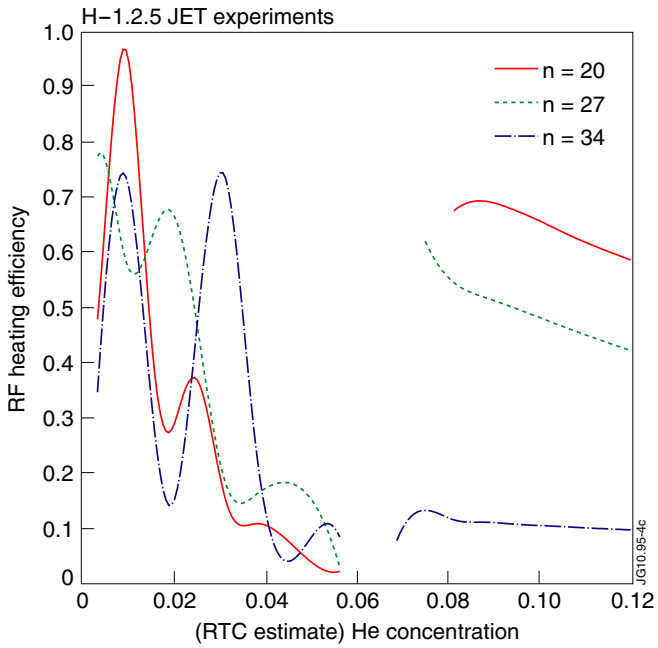

Figure 17. Total ICRF heating efficiency as a function of the ^{3}He concentration for three toroidal mode numbers in the main lobe of the vacuum dipole spectrum.

largely for geometrical reasons since both the MC and the cyclotron layers are located at $R \sim$ constant surfaces and thus a given major radius position contributes to the energy deposited on various magnetic surfaces. Simply accounting for that 'geometrical spreading' factor $(1-(Z/a_p)^2)^2$ on the 1D results yields the wing-like depositions with a sharp rise toward the core and a more shallow decrease toward the edge; the position at which the maximum absorption is reached is accurately predicted by the 1D wave equation solver, as can easily be seen glancing at figure 16(*d*) depicting the 1D TOMCAT deposition profile as a function of the magnetic surface label ρ (=half the width of the magnetic surface in the equatorial plane). A more important issue missed entirely by the 1D description is the fact that wave interference is somewhat moderated when the full geometry and wave sloshing over the vessel is accounted for, which tends to smoothen the deposition profiles and yields less pronounced interference patterns when summing over all (coupled) poloidal and (decouped) toroidal modes of the wave spectrum. Also the delicate competition between the temperature and poloidal field effects is outside the scope of the 1D description. Figure 19 shows the 2D parallel electric field component computed by the TORIC code for $X[^3\text{He}] = 5\%$ (left figure) and $X[^3\text{He}] = 17\%$ (right figure) consistent with the dispersion equation root shown in figure 15. The D-like species constitute 30% of the density, the toroidal magnetic field is 3.41 T and the plasma current is 1.8 MA while the ICRH frequency taken is 32.25 MHz; rather than accounting for the full antenna spectrum only the dominant toroidal mode number for dipole phasing of the antennas ($n = 27$) was picked. The corresponding FW dispersion (showing where the confluence and cutoff positions are located) is depicted in figure 15. For the lower ^{3}He concentration case, the FW is facing 2 MC layers while for the higher ^{3}He concentration case, one of these layers has moved out of the plasma on the low magnetic field side. In the central region the temperature is high so there is a clear competition between the Bernstein and ion cyclotron mode: In line with the interpretation of Perkins [37], the $k_\parallel$-shift due to poloidal field effects is minimal in the equatorial plane which gives rise to the excitation of the ion Bernstein wave propagating away from the confluence at $x = R - R_o \sim -0.1$ m toward the HFS. Away from the equatorial plane, the poloidal field effects dominate, which results in the excitation of the ion cyclotron wave propagating toward the low rather than the high field side. At the confluence layer in the lower temperature region (at $x = R - R_o \sim 0.55$ m) the poloidal field effects dominate and only the ion cyclotron wave is excited, hence no short wavelength structure is observed at $x < 0.55$ m. Except for the fact that the core MC layer has shifted further to the HFS and that the electric field amplitudes differ, the electric field pattern of the $X[^3\text{He}] = 17\%$ case in the core is similar to that of the $X[^3\text{He}] = 5\%$ case. As corroborated by the dispersion equation figure (figure 15), the other MC has now disappeared from the plasma. Note that there is also a trace of wave structure at the far HFS: a small fraction of the wave power manages to tunnel through the wide FW evanescence layer at the HFS and encounters a supplementary confluence close to the plasma edge ($x \sim -0.9$ m) also noticeable in figure 15.

Since both minority and MC heating allow efficient heating, a critical issue regarding its application in ITER is whether the MC–cutoff pair that approaches the LFS edge and that compromises the RF performance in a limited $X[^3\text{He}]$ interval can occur in that machine. A dispersion and 1D wave equation analysis allows us to readily show that—in view of ITER's size and plasma composition—only unrealistically high $X[^3\text{He}]$ could cause this problem to occur. On the other hand, the fact whether the interference effect would be important or not critically depends on the temperature, i.e. on the single pass absorption through individual conversion/damping layers.

4. Conclusions

The recent JET experiments have shown that MC heating can be as efficient as minority heating in (^{3}He)–H plasmas. The experimental heating efficiency varied from 0.3 to 0.7. The possibility to enhance the MC efficiency by properly tuning the plasma parameters was examined.

The heating efficiency at the various ^{3}He concentrations was found to be intimately related to the MC layers residing in the plasma. At very low ^{3}He concentrations ($X[^3\text{He}] < 2\%$) fast ^{3}He ions testify for efficient minority heating although the bulk ion response was never observed to be significant. The electrons, however, react promptly to steps in the ICRF power level used to determine the experimental power deposition profile. At ^{3}He concentrations of ~5%, poor ICRF coupling gave rise to poor heating performance. Analysis linked this reduced performance to a MC layer crossing the LFS edge, a wide evanescence layer being present in front of the antenna, hindering waves to penetrate the plasma. At still higher concentrations, just 1 rather than 2 MC layers lie inside the

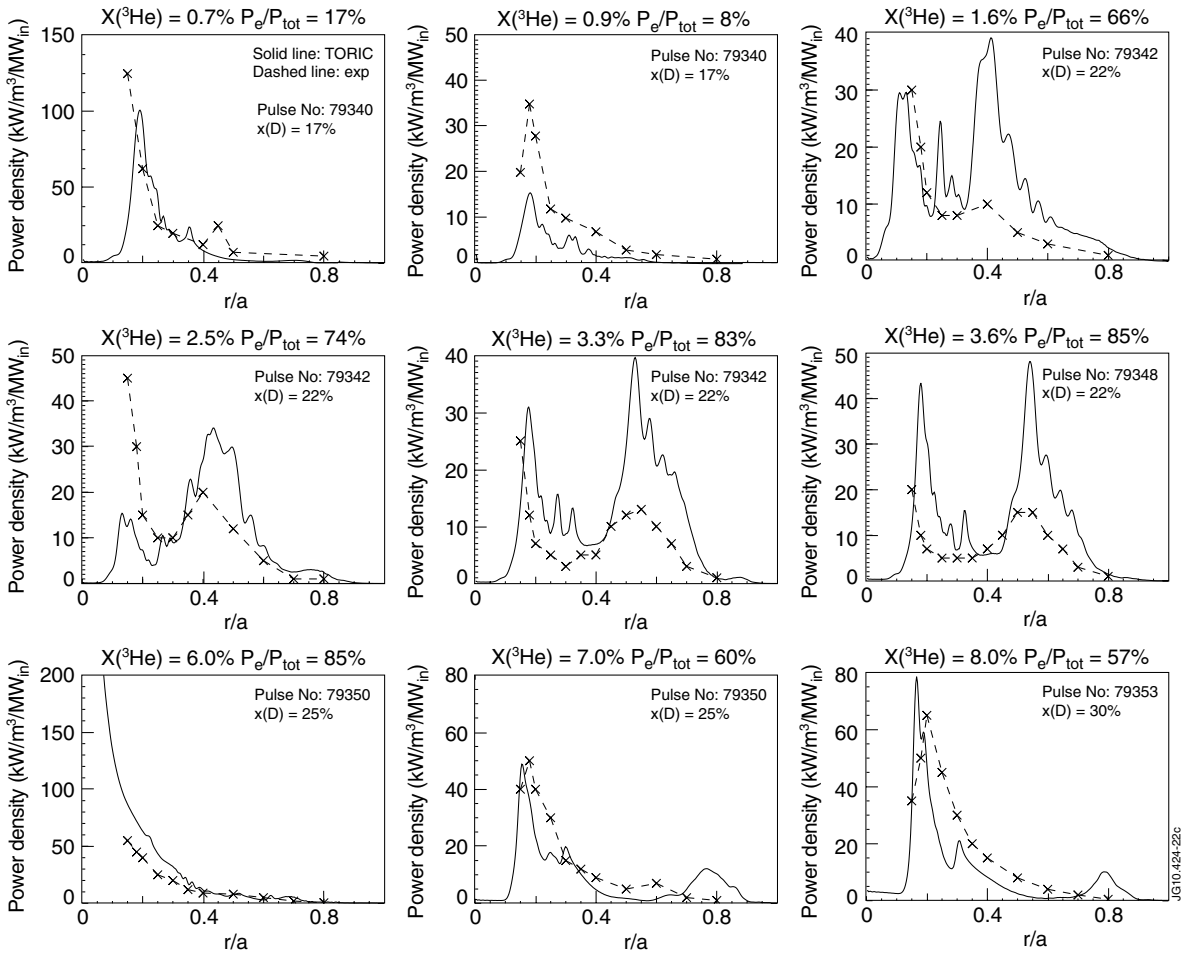

Figure 18. ICRF electron power deposition profile found by TORIC using experimental density and temperature values (solid lines), and experimental electron deposition profiles (dashed line with crosses).

plasma. This results in increased heating efficiency, less sensitive to the actual ^{3}He concentration and similar to the efficiencies observed in non-inverted (^{3}He)–D plasmas.

The different behavior in the 2 MC regimes could be explained with the constructive/destructive interference scheme e.g. proposed by Fuchs [33] and its generalization to two resonance/MC layers by Kazakov [35]. Provided the plasma constituents are well known, minute changes in the most relevant parameters ($X[^3\text{He}]$, B_o, antenna phase) allow one to tune the heating scheme to optimize the heating efficiency. The experiments discussed in this paper have, however, underlined that this tuning might not be straightforward if the relation between the impurity influx and wave related processes in the plasma edge and scrape-off layer is not well characterized: as already noticed by Mayoral [4], D-like ions have a non-negligible impact on the position of MC layers in inverted scenarios. Although some plasma constituents may themselves not be heated by the ICRF waves, they can have a considerable impact on the RF field pattern and polarization and thus on the RF heating efficiency.

Conforming to theory, the electron response is much more prominent than the ion response. Also, subpopulations of fast particles were created: At very low ^{3}He concentrations the signature of very fast ICRF accelerated ions was seen in the fast ion loss detector and the gamma ray detector. At high ^{3}He concentrations, fast ^{3}He particles were no longer observed but fast D and ^{4}He populations were detected by various diagnostics, in spite of the fact that electron heating is aimed for at these high concentrations. The neutron rate—resulting from colliding ICRF accelerated D neutral beam particles and thus intimately related to the use of D beams—rose to a level of 10^{14} neutrons per second at high ^{3}He concentration while the neutrons are virtually absent at low ^{3}He concentration. ICRF heated D beam particles are accelerated to energies of $\sim$250 keV. The fast ^{4}He observed are likely not RF heated ^{4}He but α-particles arising from the nuclear reaction D(^{3}He,p)^{4}He.

In conclusion, both the fundamental ^{3}He minority cyclotron as the MC heating scheme (reached when increasing the minority concentration level above a few per cent) perform well in (^{3}He)–H plasmas. These two schemes are the only RF heating schemes available for ITER's full field non-activated phase in H plasmas. Whereas a confluence and associated cutoff near the edge compromised the JET experiments when $X[^3\text{He}]$, dispersion equation and 1D analysis reveals that this is not an issue for ITER plasmas.

Acknowledgments

This work, supported by the European Communities under the contract of the Association between EURATOM and the

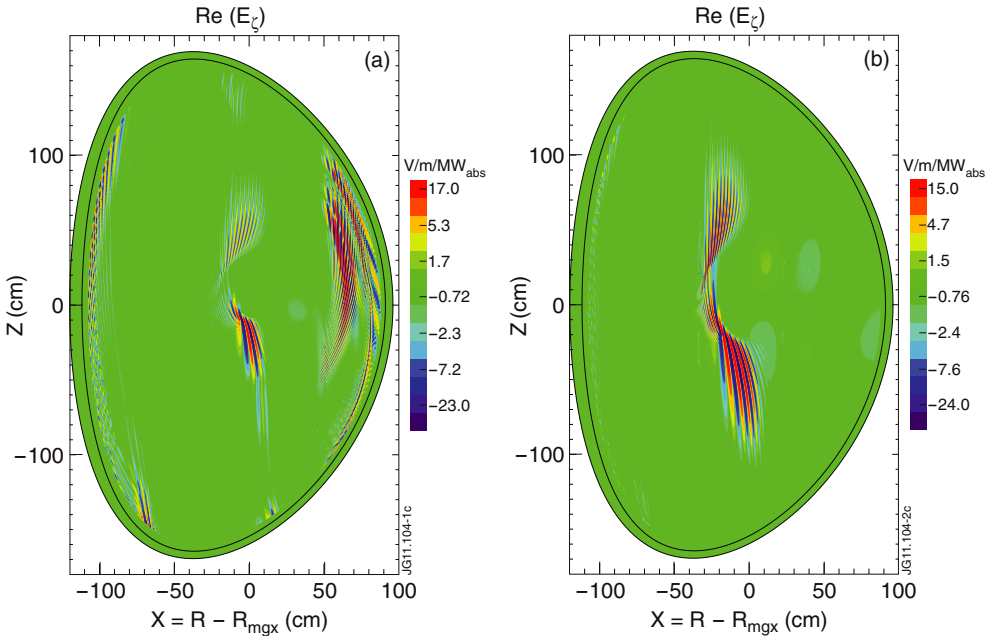

Figure 19. Parallel electric field component for $X[^3\mathrm{He}] = 5\%$ (left) and $X[^3\mathrm{He}] = 17\%$.

Belgian State, was carried out within the framework of the European Fusion Development Agreement. The views and opinions expressed herein do not necessarily reflect those of the European Commission.

References

[1] Lerche E *et al* 2010 Experimental investigation of ICRF heating scenarios for ITER's half-field phase performed in JET *37th EPS Conf. on Plasma Phys. (Dublin, Ireland, 2010)* paper O4.12

[2] Lerche E *et al* 2012 Experimental investigation of ion cyclotron range of frequency heating scenarios for ITER's half field Hydrogen phase performed in JET *Plasma Phys. Control. Fusion* **54** 074008

[3] Van Eester D *et al* 2002 *Nucl. Fusion* **42** 310–28

[4] Mayoral M-L *et al* 2006 *Nucl. Fusion* **46** S550–S563

[5] Intrator T *et al* 1996 *Phys. Plasmas* **3** 1331

[6] Majeski R *et al* 1996 *Phys. Rev. Lett.* **76** 764–7

[7] Nguyen F *et al* 2002 *29th EPS Conf. on Plasma Physics and Controlled Fusion (Montreux, Switzerland, 17–21 June 2002)* vol 26B (ECA) paper P-1.045

[8] Noterdaeme J-M *et al* 1999 *Proc. 26th Conf. on Controlled Fusion and Plasma Physics (Maastricht, The Netherlands)* vol 23J (ECA) pp 1561–4

[9] Nelson-Melby E *et al* 2003 *Phys. Rev. Lett.* **90** 155004

[10] Lin Y *et al* 2005 *Plasma Phys. Control. Fusion* **47** 1207–28

[11] Van Eester D *et al* 2009 *Plasma Phys. Control. Fusion* **51** 044007

[12] Saoutic B *et al* 1996 *Phys. Rev. Lett.* **76** 1647

[13] Monakhov I *et al* 1999 *Phys. Plasmas* **6** 885–96

[14] Vukovic M *et al* 1996 Evidence of coupling to global Alfvén eigenmodes during Alfvén wave current drive experiments on the Phaedrus-T tokamak *AIP Conf. Proc.* **355**, *11th Topical Conf. on Radio Frequency Power in Plasmas (Palm Springs, CA, 17–19 May 1995)* 471–4

[15] Mantica P *et al* 2006 *Phys. Rev. Lett.* **96** 095002

[16] Lin Y 2010 ICRF mode conversion flow drive in JET D-(^{3}He) plasmas and comparison with results from Alcator C-Mod *37th EPS Conf. on Plasma Physics (Dublin, Ireland)* paper P5.164

[17] Lerche E *et al* 2008 *Plasma Phys. Control. Fusion* **50** 035003

[18] Mantsinen M *et al* 2008 private communication

[19] Hellesen C *et al* 2010 *Rev. Sci. Instrum.* **81** 10D337
Hellesen C 2010 Diagnosing fuel ions in fusion plasmas using neutron emission spectroscopy *PhD Thesis* Uppsala University

[20] Kiptily V *et al* 2012 Fast ions in mode conversion heating (^{3}He)–H plasma in JET *Plasma Phys. Control. Fusion* **54** 074010

[21] Korotkov A A *et al* 1997 *Nucl. Fusion* **37** 35–51

[22] Gatu Johnson M *et al* 2008 *Nucl. Instrum. Methods* A **591** 417

[23] Hellsten T *et al* 2012 Observation of rotation in JET plasmas with electron heating by ion cyclotron resonance heating *Plasma Phys. Control. Fusion* **54** 074007

[24] Lin Y *et al* 2012 Ion cyclotron range of frequency mode conversion flow drive in D(^{3}He) plasmas on JET *Plasma Phys. Control. Fusion* **54** 074001

[25] Heikkinen J A, Hellsten T and Alava M J 1979 *Nucl. Fusion* **31** 417–30

[26] Lamalle P U 1994 Nonlocal theoretical generalization and tridimensional study of the coupling of an ICRH antenna to a tokamak plasma *PhD Thesis* LPP-ERM/KMS Report 101, Université de Mons

[27] Dumont R J 2009 *Nucl. Fusion* **49** 075033

[28] Brambilla M 1988 *Nucl. Fusion* **28** 549

[29] Van Eester D *et al* 1998 *Plasma Phys. Control. Fusion* **40** 1949–75

[30] Budden K G 1961 *Radio Waves in the Ionosphere* (Cambridge: Cambridge University Press)

[31] Swanson G 1983 *Handbook of Plasma Physics: Basic Plasma Physics I* ed M N Rosenbluth and R Z Sagdeev (Amsterdam: North-Holland)

[32] Faulconer D 1980 *Phys. Lett.* A **75** 355

[33] Fuchs V *et al* 1995 *Phys. Plasmas* **2** 1637–47

[34] Kazakov Ye *et al* 2010 *Plasma Phys. Control. Fusion* **52** 115006

[35] Kazakov Ye *et al* in preparation

[36] Karney C F F, Perkins F W and Sun Y-C 1979 *Phys. Rev. Lett.* **42** 1621–4

[37] Perkins F W 1977 *Nucl. Fusion* **17** 1197